Basin Research (2006) **18**, 1–26, doi: 10.1111/j.1365-2117.2006.00283.x

Propagation of orographic barriers along an active range front: insights from sandstone petrography and detrital apatite fission-track thermochronology in the intramontane Angastaco basin, NW Argentina

Isabelle Coutand,*† Barbara Carrapa,† Anke Deeken,‡ Axel K. Schmitt,§ Edward R. Sobel† and Manfred R. Strecker†

*Université des Sciences et Technologies de Lille 1, UMR-CNRS 8110, UFR des Sciences de la Terre (bât.SN5), Villeneuve d'Ascq cedex, France
†Universität Potsdam, Institut für Geowissenschaften, Potsdam, Germany
‡Institut für Geowissenschaften, Freie Universität Berlin, Maltesestrasse, Berlin, Germany
§Department of Earth and Space Sciences, University of California, Los Angeles, CA, USA

ABSTRACT

The arid Puna plateau of the southern Central Andes is characterized by Cenozoic distributed shortening forming intramontane basins that are disconnected from the humid foreland because of the defeat of orogen-traversing channels. Thick Tertiary and Quaternary sedimentary fills in Puna basins have reduced topographic contrasts between the compressional basins and ranges, leading to a typical low-relief plateau morphology. Structurally identical basins that are still externally drained straddle the eastern border of the Puna and document the eastward propagation of orographic barriers and ensuing aridification. One of them, the Angastaco basin, is transitional between the highly compartmentalized Puna highlands and the undeformed Andean foreland. Sandstone petrography, structural and stratigraphic analysis, combined with detrital apatite fission-track thermochronology from a ~6200-m-thick Miocene to Pliocene stratigraphic section in the Angastaco basin, document the late Eocene to late Pliocene exhumation history of source regions along the eastern border of the Puna (Eastern Cordillera (EC)) as well as the construction of orographic barriers along the southeastern flank of the Central Andes.

Onset of exhumation of a source in the EC in late Eocene time as well as a rapid exhumation of the Sierra de Luracatao (in the EC) at about 20 Ma are recorded in the detrital sediments of the Angastaco basin. Sediment accumulation in the basin began ~15 Ma, a time at which the EC had already built sufficient topography to prevent Puna sourced detritus from reaching the basin. After ~13 Ma, shortening shifted eastward, exhuming ranges that preserve an apatite fission-track partial annealing zone recording cooling during the late Cretaceous rifting event. Facies changes and fossil content suggest that after 9 Ma, the EC constituted an effective orographic barrier that prevented moisture penetration into the plateau. Between 3.4 and 2.4 Ma, another orographic barrier was uplifted to the east, leading to further aridification and pronounced precipitation gradients along the mountain front. This study emphasizes the important role of tectonics in the evolution of climate in this part of the Andes.

INTRODUCTION

The Altiplano-Puna plateau stretches for ~2000 km from southern Peru to northwestern Argentina and is a first-order topographic feature of the Central Andes. The plateau is bounded on the west by active stratovolcanoes of the Western Cordillera and on the east by the basement-involved thrust system of the Eastern Cordillera (EC) (Fig. 1a and b). Both Cordilleras reach elevations in excess of 6500 m and delimit the plateau region of 3800 m average elevation. The present-day elevation of the plateau is commonly attributed to crustal thickening in the course of distributed tectonic shortening (e.g. Isacks, 1988; Allmendinger *et al.*, 1997; Lamb *et al.*, 1997; Kley & Monaldi, 1998; McQuarrie, 2002), and subsequent wholesale uplift following delamination of mantle lithosphere in its southern part (Argentinian Puna) (Kay *et al.*, 1994; Allmendinger *et al.*, 1997).

Correspondence: Isabelle Coutand, Université des Sciences et Technologies de Lille 1, UMR-CNRS 8110, UFR des Sciences de la Terre (bât. SN5), 59655 Villeneuve d'Ascq cedex, France. E-mail: isabelle.coutand@univ-lille1.fr

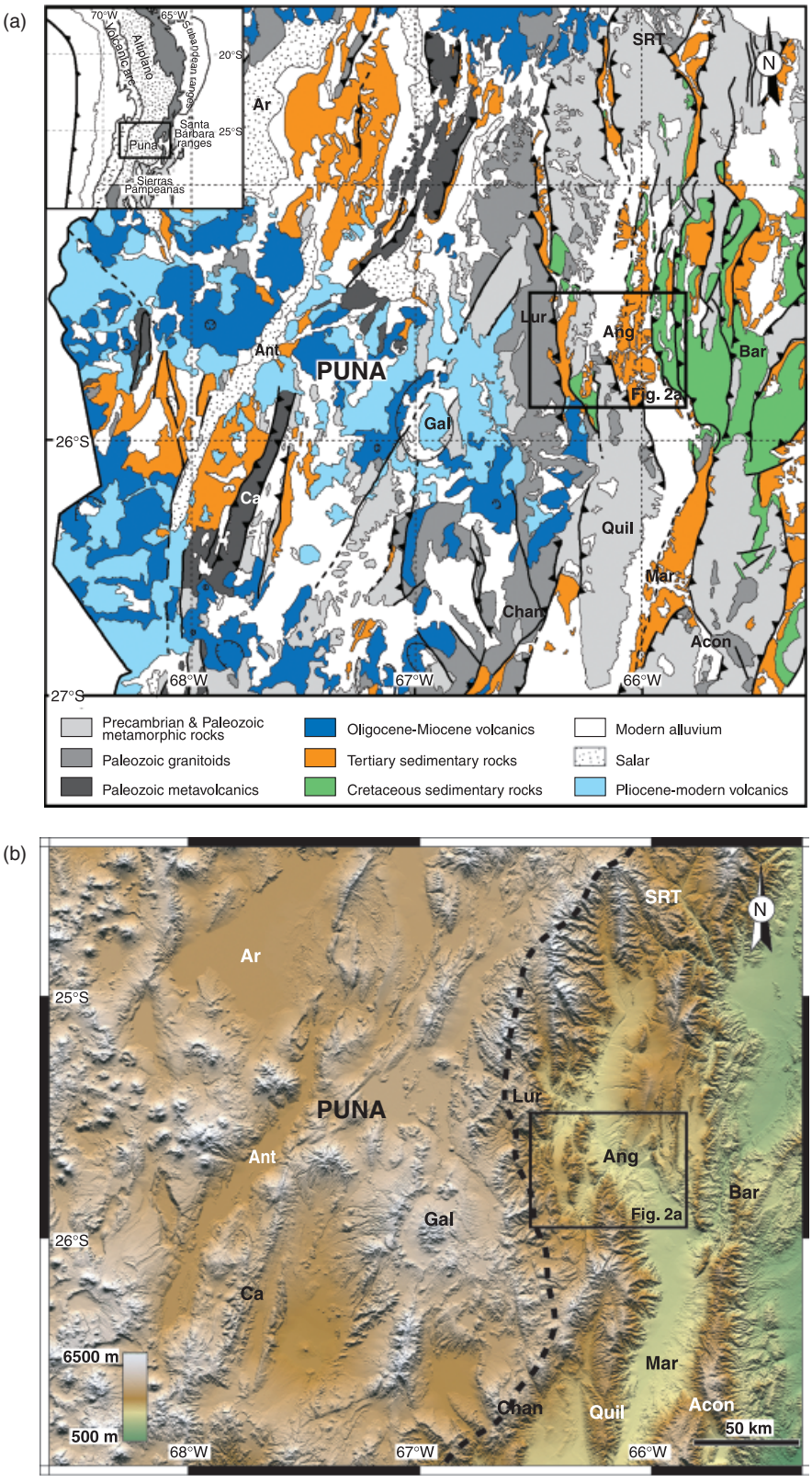

Fig. 1. (a) Geological map of the southeastern Central Andes (redrawn from the geological maps of Salta, Catamarca and Tucuman provinces, scale 1 : 500 000). (b) DEM of the southern central Andes between 24–27°S and 69–64°W. Data are from SRTM 90-m square-grid DEM. The heavy dashed line shows the boundary between the internally drained Puna plateau and the foreland areas that drain to the east. (c) Coloured mean annual precipitation distribution along the southeastern Central Andes based on data from WMO (1975) and Bianchi & Yañez (1992). Location of (a–c) is given by the black square in inset (a). Abbreviations are Acon, Aconquija range; Ang, Angastaco basin; Ant, Antofalla salar; Ar, Arizaro salar; Bar, Santa Barbara ranges; Ca, Calalaste range; Chan, Chango Real range; OC, Oire intrusive complex; Gal, Cerro Galán; Lur, Cumbres de Luracatao; Mar, Santa Maria valley; Quil, Quilmes range; SRT, Santa Rosa de Tastíl.

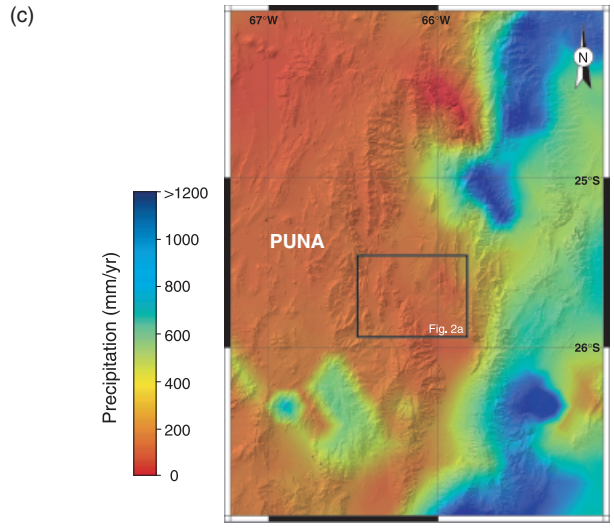

Fig. 1. Continued

The Puna plateau comprises internally drained, partially overfilled contractional basins where up to 6000 m of late Eocene to Pliocene continental clastics and evaporites have accumulated (Jordan & Alonso, 1987; Kraemer *et al.*, 1999; Adelmann, 2001; Coutand *et al.*, 2001). These basins are thrust-bounded and isolated from each other by ~N–S trending basement ranges, typically 1000–1500 m higher than the plateau floor (Coutand, 1999; Coutand *et al.*, 2001 and references therein) (Fig. la and b). The deposition of thick evaporite units is related to internal drainage and sustained aridity, at least during the last 27–14 Myr (Alonso *et al.*, 1991; Vandervoort *et al.*, 1995; Adelmann, 2001; Carrapa *et al.*, 2005). The aridity results from the latitudinal position in a region of descending air masses (e.g. Hartley, 2003; R. Alonso, B. Carrapa, I. Coutand, M. Haschke, G.E. Hilley, E.R. Sobel, M.R. Strecker & M.H. Trauth, submitted) and the condensation of Atlantic-derived moisture along the eastern (windward) flank of the orogen (e.g. Masek *et al.*, 1994; Haselton *et al.*, 2002) (Fig. lc).

Sobel *et al.* (2003) and Hilley & Strecker (2005) have suggested a model for the Puna plateau and adjacent regions in which the low internal relief, aridity and internal drainage are intimately linked and have persisted in this region because tectonic uplift has overwhelmed the inefficient fluvial system and caused orogen-traversing channels to be defeated, thus disconnecting the interior of the orogen from the foreland base level. The combination of an arid climate and tectonic activity along range fronts implies that progressive aridification of the hinterland is promoted when laterally continuous orographic barriers along the margin of the plateau are perpendicular to moisture-bearing winds. If aridity is coupled with low erodibility, and moderate to high uplift rates of orographic barriers, the channel network draining the hinterland will be fragmented. Consequently, material removed from the leeward side of the uplifts will fill internally drained basins. The failure of erosional mass export will increase gravitational stresses in the hinterland and eventually promote the migration of contractional deformation into the foreland, advancing orographic barriers and precipitation in the same direction (Sobel & Strecker, 2003; Sobel *et al.*, 2003; Hilley & Strecker, 2004).

To further evaluate this model and to understand the upper crustal and surficial mechanisms that promote the formation, maintenance and lateral growth of a high plateau, it is important to better constrain the space–time development of orographic barriers. Most estimates for the timing of shortening and associated crustal thickening and surface uplift in NW Argentina rely on the synorogenic record of contractional basins within and adjacent to the orogenic belt (Jordan & Alonso, 1987; Strecker *et al.*, 1989; Allmendinger *et al.*, 1997; Jordan *et al.*, 1997; Kraemer *et al.*, 1999; Coutand *et al.*, 2001). However, across and at the border of the southern Puna, little is known about (1) the onset of tectonic shortening as a proxy for mountain building and (2) the spatial distribution and propagation of contractional deformation through time. Whereas some argue that the propagation of the contractional front was uniform in space from west to east with shortening starting within the plateau in the early Miocene (~15–20 Ma) (Jordan & Alonso, 1987; Allmendinger *et al.*, 1997) and reaching the plateau margin by the late Miocene (10–6 Ma) (Strecker *et al.*, 1989; Allmendinger *et al.*, 1997; Marrett & Strecker, 2000), other studies suggest that early contraction and uplift occurred within and at the eastern periphery of the plateau as early as the late Eocene–Oligocene time (Kraemer *et al.*, 1999; Adelmann, 2001; Coutand *et al.*, 2001; Carrapa *et al.*, 2005), similar to observations made to the north in the Bolivian Andes (Horton *et al.*, 2002; Horton, 2005).

In this study, we evaluate the tectono-sedimentary history of the southeastern Puna margin by reconstructing the evolution of the intramontane Angastaco basin, located between the plateau and eastern foreland ranges. The Angastaco basin is part of the semi-arid Calchaquí Valley receiving ~200 mm of rainfall annually; it is thus trapped between the arid Puna plateau to the west ($\leq 100\,mm\,yr^{-1}$) and the humid Chaco lowlands of the Andean foreland to the east ($1200\,mm\,yr^{-1}$) (Haselton *et al.*, 2002) (Fig. lc). Our new structural, sedimentologic, provenance and detrital apatite fission-track data from the Neogene Angastaco basin help reconcile different views on the timing of plateau evolution and constrain the Cenozoic structural and palaeoecologic evolution of the southeastern plateau margin. We demonstrate that contractional deformation began in the late Eocene, similar to other areas on the southern Puna plateau. Furthermore, we show that the migration of compressional deformation and related building of orographic barriers focused precipitation on the eastern, windward flanks of ranges east of the Puna. This starved the western hinterland of moisture and thus promoted the maintenance of internally drained areas in the plateau and the creation of transient internally drained basins in the transition between the plateau border and the foreland.

REGIONAL GEOLOGICAL SETTING

The narrow, N–S trending Angastaco basin is located in the distal part of a once contiguous Palaeogene Retroarc Foreland basin (Jordan & Alonso, 1987) (Fig. 1a). The reverse-fault-bounded basin is located in the semi-arid Calchaquí valley between the EC to the west, and the foreland ranges of the Santa Barbara structural province to the east, an inverted Cretaceous extensional province (Grier *et al*., 1991; Mon & Salfity, 1995) (Fig. 1a and b). On the west, the basin is overthrust by late Proterozoic to early Cambrian metasediments of the Puncoviscana Formation (Fig. 2a and b), and to the east it is limited by outcrops of Cretaceous coarse clastic rift-related sediments (Marquillas *et al*., 2005). The Angastaco basin fill comprises continental clastic deposits of the late Palaeogene to Neogene Payogastilla Group (Díaz & Malizzia, 1983), which is tilted eastward and gently folded (Fig. 2b).

The Puncoviscana Formation contains low-grade metamorphosed sandstones and shales (Turner, 1960; Toselli, 1990; Durand, 1992) that grade southward into schists, gneisses and migmatites (La Paya Fm. and Tolombón complex). These units are intruded by Cambrian to Ordovician granites (Lork *et al*., 1990; Lork & Bahlburg, 1993; Omarini *et al*., 1999). Further west, the north–south-oriented Oire intrusive complex of Ordovician granites and granodiorites crops out (Méndez *et al*., 1973; Omarini *et al*., 1984; Lork & Bahlburg, 1993) (Figs 1a and 2a). These basement lithologies constitute the source for the Payogastilla Group. The basement rocks are unconformably overlain by the rift-related Neocomian to early Eocene strata of the Salta Group (Bianucci *et al*., 1981; Grier *et al*., 1991; Salfity & Marquillas, 1994).

The Payogastilla Group (Díaz & Malizzia, 1983) rests unconformably on these units and consists of four formations (Figs 2a, b and 3): (1) the basal Quebrada de los Colorados Formation comprises sequences of coarse-grained sandstones (sometimes conglomeratic) that grade upward into fine- to medium-grained sandstones and siltstones with palaeosols (Díaz *et al*., 1987; Grier, 1990), interpreted to be alluvial plain deposits (Díaz & Malizzia, 1983). Its age is poorly constrained as either early Miocene (Díaz *et al*., 1987) or Oligocene (Starck & Vergani, 1996). In the Angastaco basin, the base of the formation is not exposed because of faulting along the eastern side of Cerro Negro (Fig. 2a and b), but the unit is 340-m thick in the Pucará valley in the west (Ruiz, 1993). (2) The unconformably overlying 4200-m-thick Angastaco Formation is composed of grey to beige conglomerates, sandstones and muddy siltstones organized in upward-fining fluvial cycles. In the lower and upper parts of the section, sandy and silty textures dominate and the sequence is interpreted as a braided stream system typical of a piedmont plain (Díaz & Malizzia, 1983) (Fig. 3). In the middle part of the section, conglomeratic lenses intercalated with coarse-grained sandstones and massive conglomeratic layers increase, indicating a distal to proximal alluvial fan origin (Díaz & Malizzia, 1983; Díaz *et al*., 1987; Díaz & Miserendino Fuentes, 1988). The virtual absence of fossils and the presence of desiccation polygons suggest that these strata may have been deposited under arid to semi-arid conditions similar to coeval units in the Santa María basin to the south (Díaz & Malizzia, 1983; Díaz & Miserendino Fuentes, 1988; Bossi *et al*., 2001; Starck & Anzótegui, 2001). A tuff at the base of the Angastaco Formation dated by the $^{40}Ar/^{39}Ar$ method on biotite yielded an age of 13.4 ± 0.4 Ma (Grier & Dallmeyer, 1990), indicating a middle Miocene age. (3) The Palo Pintado Formation is conformable with the underlying Angastaco Formation and can be divided into two parts (Fig. 3). The lower 1500 m consist of fine- to coarse-grained sandstones interlayered with siltstones and mudstones, interpreted as meandering river deposits locally with wetland facies (Díaz & Malizzia, 1983; Díaz & Miserendino Fuentes, 1988). The upper 450 m comprise an upward-coarsening succession of coarser-grained sandstones interfingered with massive conglomeratic strata and intercalated tuff beds, interpreted as braided stream deposits (Díaz & Malizzia, 1983; Díaz & Miserendino Fuentes, 1988). Mammal fossils in the lower section indicate a late Miocene to early Pliocene age and palaeoenvironments characterized by relative humidity (Marshall *et al*., 1983; Anzótegui, 1998; Starck & Anzótegui, 2001). A volcanic ash at the top of this unit (sample AI29, Fig. 3) yielded a U–Pb zircon age of 5.27 ± 0.28 Ma (see the next section). (4) Finally, the San Felipe Formation covers the Palo Pintado strata and consists of 650-m-thick conglomeratic upward-fining sequences (Grier, 1990), interpreted as braided stream deposits transitional with distal alluvial fan deposits (Díaz & Malizzia, 1983; Díaz & Miserendino Fuentes, 1988). Capped by an angular unconformity, these units are overlain by gravels that contain recycled pyroclastic material at the base, 2.4 Ma old (M. R. Strecker, unpubl. data).

U–PB ZIRCON DATING

To better constrain the stratigraphic age of the Neogene sediments of the Angastaco basin, an ash located at the top of the Palo Pintado Formation was dated by the U–Pb method on zircons (Table 1). Epoxy grain mounts of hand-selected zircons were sectioned to expose grain interiors and polished with 1 μm Al_2O_3. After ultrasonic cleaning with soapy water, diluted HCl and distilled water, the Au-coated mounts were transferred into a high vacuum chamber ($> 10^{-8}$ Torr) and kept overnight. Zircon analysis was performed using the UCLA Cameca ims 1270 ion microprobe with a mass-filtered, $\sim$15 nA $^{16}O^-$ beam focused to an $\sim$30–35 μm diameter spot. The analysis surface was flooded with O_2 at a pressure of $\sim 4 \times 10^{-3}$ Pa to enhance Pb^+ yields. Secondary ions were extracted at 10 kV with an energy band pass of 50 eV. Following a 4 min pre-sputter period to reduce surface contamination intensities for $^{94}Zr_2O^+$, $^{204}Pb^+$, $^{206}Pb^+$, $^{207}Pb^+$, $^{208}Pb^+$, $^{238}U^+$, $^{232}Th^{16}O^+$ and $^{238}U^{16}O^+$ were then sequentially measured in 10 cycles at a mass resolution of $\sim$5000, which is sufficient to resolve most molecular interferences. The relative

 Basin Research, 18, 1–26

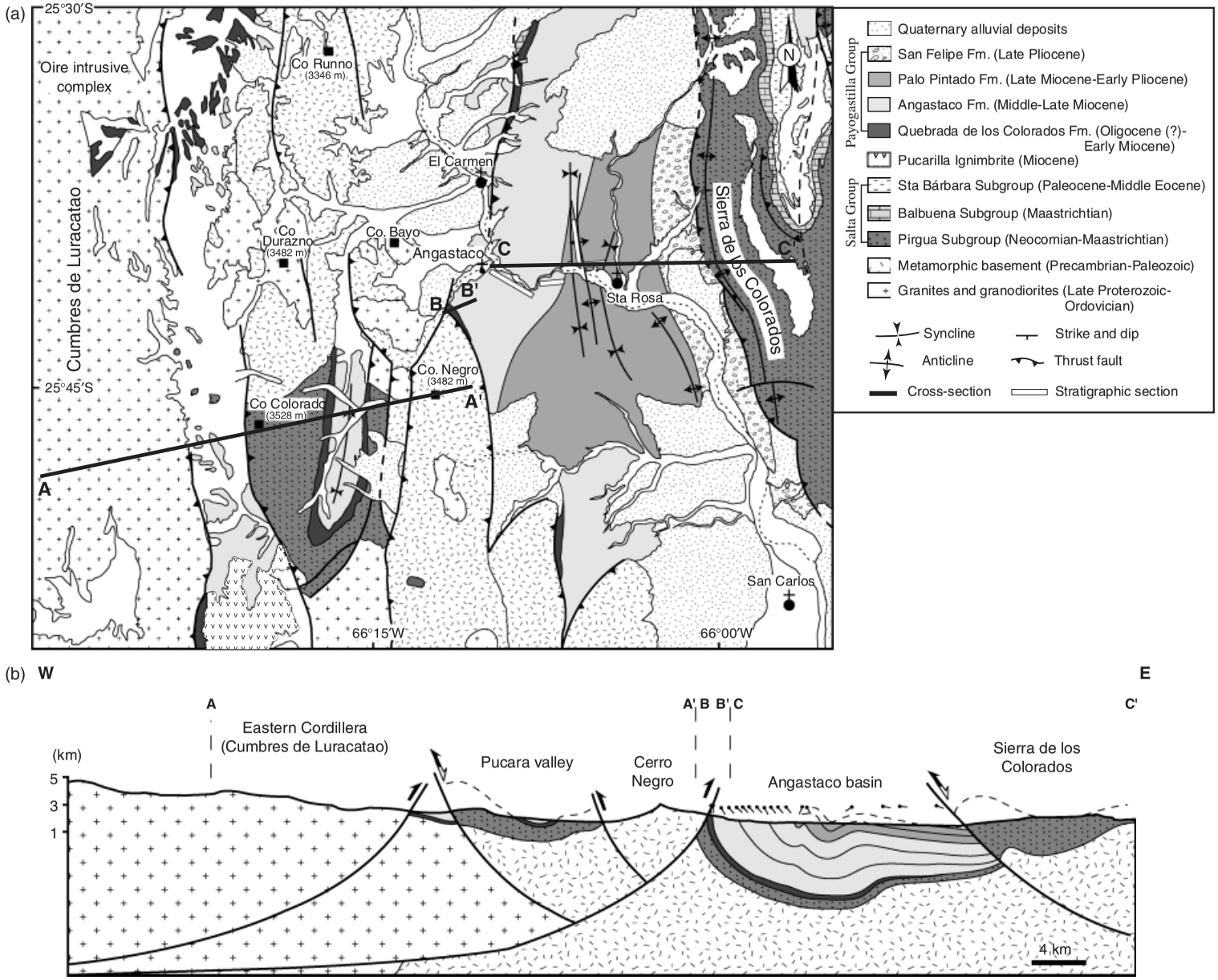

Fig. 2. (a) Geological and structural map on the Angastaco basin area (modified after Grier, 1990; Hongn *et al.*, 1999). (b) Section across the Angastaco basin area. For location and use of shading and patterns, see Fig. 2a.

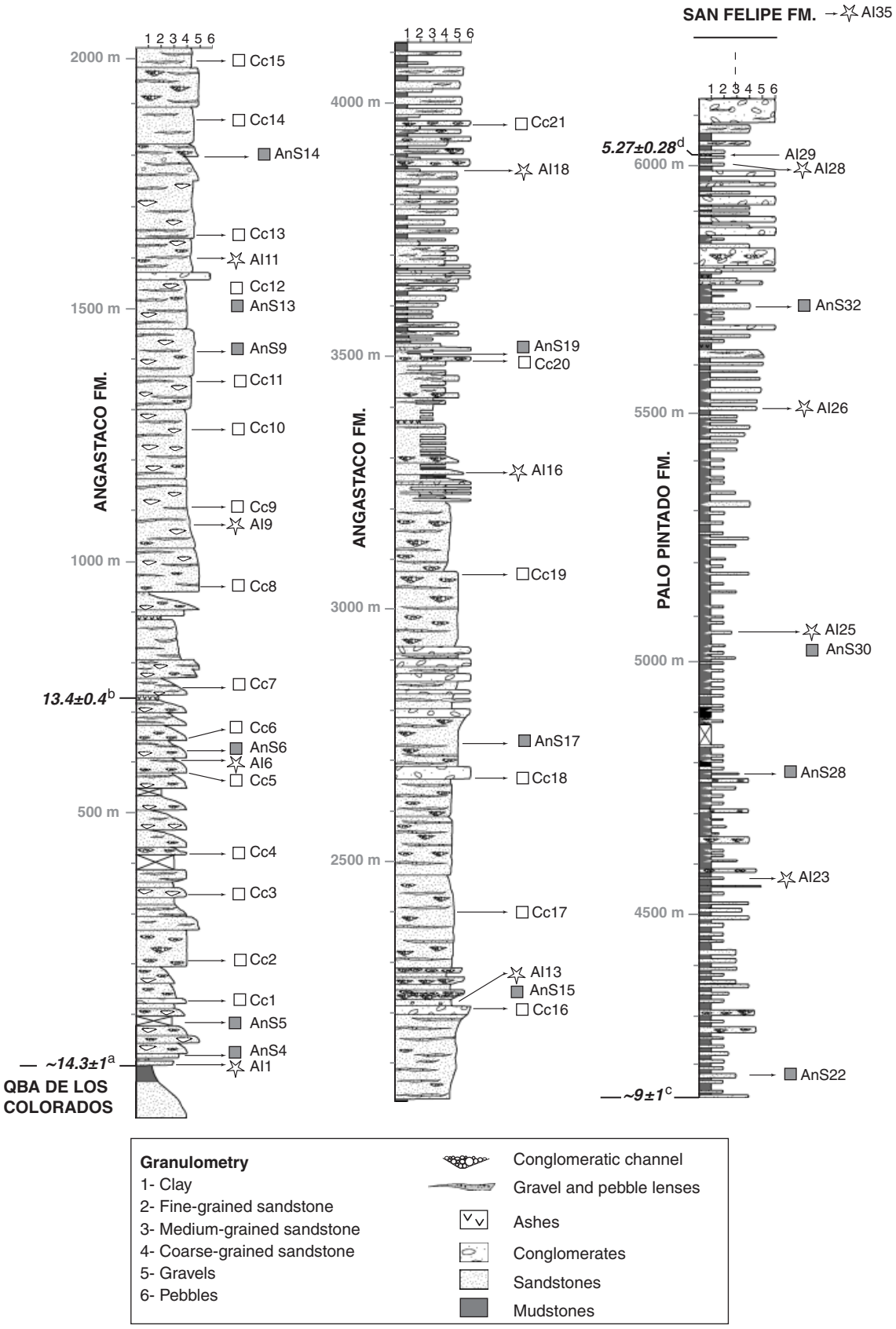

Fig. 3. Stratigraphic column of the late Neogene sedimentary fill of the Angastaco basin measured in the field (this study). Symbols are as follows: white stars indicate detrital apatite fission-track samples; grey squares, sandstone petrography samples; white squares, clast counts in conglomeratic layers. [a], age of the bottom of the Angastaco Fm., calculated from [b] and [c] assuming a constant sedimentation rate; [b], Corte El Cañon tuff dated by $^{39}Ar/^{40}Ar$ on biotite (Grier & Dallmeyer, 1990); [c], mammal fossils (Marshall *et al.*, 1983); [d], $^{206}Pb/^{238}U$ zircon age (this study).

Table 1. Zircon U–Pb results for ash AI29

Analysis	206Pb*/238U × 10^{-3}	206Pb*/238U 1 SE × 10^{-3}	207Pb*/235U × 10^{-3}	207Pb*/235U 1 SE × 10^{-3}	Correlation of concordia ellipses	207Pb corrected. disequilibrium corrected 206/238 age *t* (Ma)	1σ *t* (Ma)	Radiogenic (%)	U (p.p.m.)	Th (p.p.m.)
AI29-g1	0.9283	0.043	16.34	1.06	0.26	5.42	0.28	89.6	270	275
AI29-g2	0.9161	0.0395	20.42	3.06	0.56	5.11	0.31	85.2	535	360
AI29-g3	0.9709	0.0262	8.413	0.442	0.85	6.21	0.21	97.9	2164	827
AI29-g4	0.8209	0.0504	8.226	1.1	0.89	5.18	0.33	96.6	376	295
AI29-g5	0.8393	0.0571	6.765	0.748	0.85	5.42	0.37	98.4	2113	463
AI29-g6	0.8631	0.0499	8.23	0.608	0.50	5.49	0.32	97.1	1113	518
AI29-g7	0.7757	0.032	6.207	0.572	0.78	5.01	0.21	98.5	1229	674
AI29-g8	0.9032	0.0639	6.428	0.503	0.78	5.87	0.41	99.3	4868	2095
AI29-g9	143	2	1404	26.2	0.78	858	28	99.5	1068	120
AI29-g10	1.005	0.0156	6.53	0.146	0.83	6.54	0.22	99.9	9436	7407
AI29-g11	0.9518	0.0186	6.655	0.37	−0.10	6.18	0.20	99.4	1581	936

sensitivities for Pb and U were determined on reference zircon AS-3 (Paces & Miller, 1993) using a calibration technique similar to Compston *et al.* (1984). Th and U contents were calculated from $^{232}Th^{16}O^{+}/^{94}Zr_2O^{+}$ and $^{238}U^{16}O^{+}/^{94}Zr_2O^{+}$ with relative sensitivities calibrated on reference zircon *91500* (Wiedenbeck *et al.*, 1995), and are reported in Table 1. $^{206}Pb/^{238}U$ ages were calculated from the U–Pb isotopic ratios by linear regression and by computing the weighted average of individual results as outlined in Schmitt *et al.* (2002). In both calculation schemes, a common $^{207}Pb/^{206}Pb$ typical for anthropogenic sources was used (e.g. Sañudo-Wilhelmy & Flegal, 1994). Both methods yield ages that are in close agreement: 6.16 ± 0.42 Ma (mean square of weighted deviates MSWD = 8.4) and 5.76 ± 0.42 Ma (MSWD = 5.1; uncertainties at the 95% confidence levels with errors scaled by the square root of MSWD). The consideration that zircons from an earlier magmatic phase could be present in the sample led us to exclude some of the older zircon results (open symbols in Fig. 4, Table 1) and recalculate the ages for the younger zircon population. Excluding three older grains significantly reduces the MSWD to values close to one, and we obtained modified age estimates for AI29, which were 5.29 ± 0.27 Ma (intercept age) and 5.27 ± 0.28 Ma (weighted average age; Fig. 4). These ages are thought to represent the time of zircon crystallization in the magma that produced the AI29 ash.

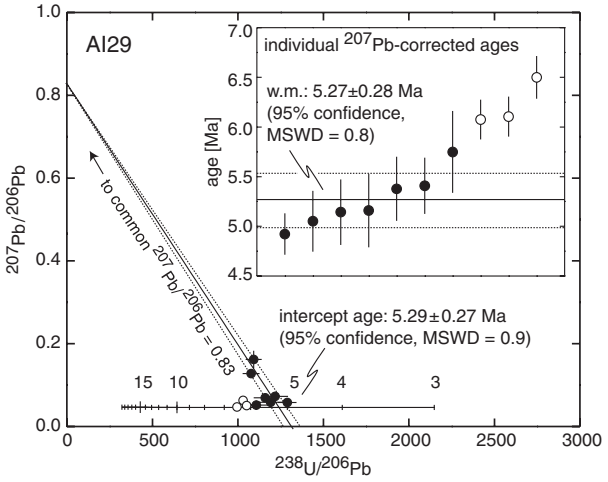

Fig. 4. $^{207}Pb/^{206}Pb$ vs. $^{238}U/^{206}Pb$ of AI29 zircons (uncorrected for common Pb; error bars 1σ). Xenocrystic zircon g9 (Table 1) has been omitted for clarity. Also note that three apparently older zircons (open symbols) have been excluded in the regression. The regression age is obtained from intersection of concordia (modified for disequilibrium assuming initial activity ratio $^{230}Th/^{238}U = 0.15$) from linear extrapolation through uncorrected data with a fixed intercept ($^{207}Pb/^{206}Pb = 0.83$). Inset shows individual ^{207}Pb-corrected ages and the weighted average age from younger zircon population ($n = 7$; solid symbols).

SANDSTONE AND CONGLOMERATE MODAL PROVENANCE ANALYSES

Method

Provenance analyses on both sandstones and conglomerates were carried out in the Angastaco and Palo Pintado Formations in order to identify different source terrains and to relate possible upsection changes to source area reorganization through time (e.g. Ingersoll *et al.*, 1984). Thirteen sandstones indicated in Fig. 3 were analysed using the Gazzi–Dickinson method (G–D) (Gazzi, 1966; Dickinson, 1970). All constituents, and at least 250 framework grains, were counted in thin sections following well-established counting procedures (Valloni, 1985; DiGiulio, 1990). We used a detailed counting form (Table 2) in order to re-calculate and present the data according to both the G–D and the Folk methods (Folk, 1968; Basu, 1976) following the procedure proposed by DiGiulio and Valloni (1992). Table 2 contains detailed information on the framework categories (quartz, feldspars and rock-lithic fragments) defin-

Table 2. Sandstone petrography results

Parameters		Formation:	Angastaco Formation								Palo Pintado Formation				
QFL+C	QFR	sample number	Ans 4	Ans 5	Ans 6	Ans 9	Ans 13	Ans 14	Ans 15	Ans 17	Ans 19	Ans 22	Ans 28	Ans 30	Ans 32
Q	Q	Quartz (QZ) straight extinction	1.9	1.2	1.6	1.9	22.5	3.2	15.1	0.4	2.0	2.4	8.1	15.5	1.4
Q	Q	QZ wavy extinction	9.9	12.4	15.0	10.5	4.1	14.9	4.2	3.8	13.1	15.2	1.8	1.3	21.7
Q	Q	Coarse polycrystalline QZ	3.5	5.1	4.1	6.1	4.7	10.6	9.6	2.5	7.5	5.9	6.0	3.3	9.6
Q	Q	Fine polycrystalline QZ	0.1	0.0	0.2	0.2	0.0	0.3	0.0	0.6	0.8	0.4	0.3	0.7	1.4
Q	R	Chert	0.0	0.0	0.0	0.0	0.0	0.0	0.0	0.0	0.0	0.0	0.0	0.0	0.0
Q	R	QZ (> 62 μm) in plutonic rock	3.6	1.6	1.2	0.5	2.0	5.2	2.1	0.3	0.8	1.4	1.0	1.3	2.0
Q	R	QZ (> 62 μm) in metamorphic rock	3.8	2.8	2.8	2.4	5.6	4.6	11.7	4.3	5.3	2.4	5.7	8.9	4.9
F	R	QZ (> 62 μm) in volcanic rock	0.1	0.0	0.0	0.0	0.0	0.0	0.0	0.2	0.2	0.0	0.0	0.0	0.0
F	F	K monocrystalline (*altered*)	4.7 *(1.9)*	12.4 *(2.6)*	8.1 *(1.3)*	8.3 *(2.2)*	16.1 *(3.5)*	15.7 *(3.7)*	7.5	4.0	7.9 *(1.8)*	10.7 *(1.2)*	9.6 *(1)*	11.5 *(3.3)*	6.7 *(0.9)*
F	R	K (> 62 μm) in plutonic rock (*altered*)	1.5 *(0.1)*	2.8 *(1)*	2.1	4.1 *(1.5)*	4.1 *(1.2)*	4.3 *(0.6)*	3.6 *(1.2)*	0.4	0.4	2.8 *(0.6)*	2.6	3 *(0.7)*	2.9
F	R	K (> 62 μm) in metamorphic rock *(altered)*	1.7	3.2	3.3	4.8	8.5 *(1.8)*	7.4	11.1 *(1.8)*	3.4	6.3	4.2	9.9 *(0.3)*	15.8 *(1.3)*	11.6
F	R	K (> 62 μm) in volcanic rock	0.0	0.0	0.0	0.0	0.0	0.0	0.0	0.0	0.0	0.0	0.0	0.0	0.0
F	F	P monocrystalline (*altered*)	1.0	0.4	1.0	0.5	2.0	0.6	1.8	1.0	1.0	0.2	0.3	2.0	0.0
F	R	P (> 62 μm) in plutonic rock	0.0	0.0	0.0	0.0	0.0	0.0	0.9	0.0	0.0	0.0	0.0	0.3	0.0
F	R	P (> 62 μm) in metamorphic rock	0.0	0.2	0.0	0.0	0.3	0.3	1.2	0.0	0.6	0.2	0.0	3.0	0.0
F	R	P (> 62 μm) in volcanic rock	0.0	0.0	0.2	0.0	0.0	0.0	0.0	0.0	0.0	0.0	0.0	0.0	0.0
Ls	R	Metamorphic lithic (with constituents < 62 μm)	2.6	4.9	1.8	4.1	5.8	4.6	8.4	6.8	7.1	5.1	20.8	17.8	13.0
Ls	R	Volcanic lithic	2.9	2.2	0.2	0.0	1.2	0.0	0.0	0.0	0.6	0.4	0.3	0.0	0.0
Ls	R	Clastic lithic	0.1	0.0	0.0	0.0	0.0	0.3	0.0	0.0	0.0	0.0	0.0	0.0	0.0
xxx	xxx	Monocrystalline biotites/chlorites	0.6	0.2	2.8	0.0	2.3	0.3	0.6	0.8	0.0	0.6	1.8	1.7	2.3
xxx	xxx	Monocrystalline muscovites	0.4	0.4	1.0	0.5	1.8	0.6	0.9	0.6	0.0	0.2	1.3	1.0	0.9
xxx	R	Mica (> 62 μm) in crystalline rock fragment	0.6	0.0	0.2	0.0	0.9	0.9	2.4	0.6	0.2	0.0	0.8	3.3	0.0
xxx	R	Mica (> 62 μm) in volcanic or clastic rock fragment	0.6	0.0	0.0	0.0	0.0	0.0	0.0	0.0	0.2	0.0	0.0	0.0	0.0
xxx	xxx	Monocrystalline heavy minerals	0.1	0.2	0.3	0.0	0.3	0.3	0.9	0.1	0.0	0.2	0.0	0.0	0.0
xxx	R	Heavy mineral (> 62 μm) in crystalline rock	0.0	0.0	0.2	0.2	0.0	0.0	0.0	0.0	0.0	0.0	0.0	0.0	0.3
xxx	R	Heavy mineral (> 62 μm) in volcanic or clastic rock	0.0	0.0	0.0	0.0	0.0	0.0	0.0	0.0	0.0	0.0	0.0	0.0	0.0
Ls	R	Calc-schist	0.0	0.0	0.0	0.0	0.0	0.0	0.0	0.0	0.0	0.0	0.0	0.0	0.0
C	R	Sparry calcite	0.0	0.0	0.7	0.0	0.0	0.0	0.0	0.0	0.2	0.0	0.0	0.0	0.0
C	R	Dolomite	0.0	0.0	0.0	0.0	0.0	0.0	0.0	0.0	0.0	0.0	0.0	0.0	0.0
C	R	Impure calcareous grain	0.0	0.0	0.0	0.0	0.0	0.0	0.0	0.0	0.0	0.0	0.0	0.0	0.0
C	R	Mudstone–wackstone	0.0	0.0	0.0	0.0	0.0	0.0	0.3	0.0	0.0	0.0	0.0	0.0	0.0
C	R	Packstone–grainstone	0.0	0.0	0.0	0.0	0.0	0.0	0.0	0.0	0.0	0.0	0.0	0.0	0.0
		Total framework grains	31.5	33.9	34.1	31.0	48.2	51.9	63.0	27.8	46.0	37.8	46.8	54.1	68.7
		Glauconite	0.0	0.0	0.0	0.0	0.0	0.0	0.0	0.0	0.0	0.0	0.0	0.0	0.0
		Pelitic clast	0.0	0.0	0.0	0.0	0.0	0.0	0.0	0.0	0.0	0.0	0.0	0.0	0.0
		Bioclast	0.0	0.0	0.0	0.0	0.0	0.0	0.0	0.0	0.0	0.0	0.0	0.0	0.0
		Altered material	3.5	3.4	8.7	1.7	2.6	0.3	4.2	1.1	2.0	4.0	3.1	1.0	3.2

	Authigenic mineral in unknown grain	0.0	0.0	0.2	0.7	0.3	0.0	0.0	0.0	0.0	0.0	0.0	0.0	0.0
	Pore in unknown grain	0.3	0.2	0.0	0.0	0.0	0.0	0.0	0.0	0.0	1.2	0.0	0.0	0.3
	Coarse silt	0.9	0.8	1.8	2.0	1.2	0.0	1.2	0.8	1.6	4.0	3.9	3.6	0.3
	Siliciclastic matrix	3.8	6.9	12.7	4.4	2.6	13.5	1.5	2.2	4.7	9.1	4.9	3.3	6.4
	Carbonate matrix	0.0	0.0	0.7	0.2	1.5	0.3	0.6	0.0	0.0	0.0	0.0	0.0	0.0
	Qz cement	0.0	0.0	0.0	0.0	0.0	0.0	0.0	0.0	0.0	0.0	0.0	0.0	0.0
	Phyllosilicate cement	10.6	7.7	22.4	2.6	7.3	5.2	8.7	4.0	6.9	4.4	0.8	1.3	3.8
	Carbonate cement	0.1	0.0	2.1	2.4	1.8	0.3	1.2	0.0	0.0	0.0	0.0	0.0	0.3
	Other cements	0.0	0.0	0.0	0.0	0.0	0.0	0.0	0.0	0.0	0.0	0.0	0.0	0.0
	Inter granular porosity	40.8	31.2	1.3	41.8	0.0	6.6	0.0	61.9	30.4	24.8	17.1	0.0	7.0
	Calcitic overgrowth	0.0	0.0	3.5	0.2	0.3	0.0	0.0	0.0	0.0	0.0	0.0	0.0	0.0
	Oversized pore	0.0	0.0	0.0	0.0	0.0	0.0	0.0	0.0	0.0	0.0	0.0	0.0	0.0
	Total rock	100	100	100	100	100	100	100	100	100	100	100	100	100
	QFL													
	Q	61	47	59	50	50	54	55	44	55	54	35	37	55
	F	24	39	35	41	41	39	34	32	30	35	34	42	28
	Ls+C	15	14	6	9	9	7	11	24	15	11	32	21	17
	Average+standard deviation													
	Q	53	6							10	45			
	F	35	6							6	34			
	Ls+C	12	6							8	21			
	QFR													
	Q	40	38	49	43	40	40	36	26	43	46	24	24	45
	F	44	47	44	48	51	54	53	51	41	43	45	56	38
	R	17	14	7	9	9	7	11	24	15	11	31	20	17
	Average+standard deviation													
	Q	39	7							12	34			
	F	49	4							7	45			
	R	12	6							8	21			
Fine lithics														
Lm	Fine QZ	1.1	5.3	1.4	xxx	3.2	5.8	xxx	xxx	1.1	5.1	2.9	4.3	xxx
Lm	Chert	0.0	0.0	6.9	xxx	0.0	0.0	xxx	xxx	0.0	0.0	0.0	0.0	xxx
Lm	Radiolarite	0.0	0.0	0.0	xxx	0.0	0.0	xxx	xxx	0.0	0.0	0.0	0.0	xxx
Lm	Quarzite	1.1	0.0	0.0	xxx	0.0	0.0	xxx	xxx	0.0	0.0	0.0	0.7	xxx
Lm	Schist QZ+biotite	14.9	13.2	9.7	xxx	19.4	25.6	xxx	xxx	10.6	7.6	5.7	17.0	xxx
Lm	Schist QZ+biotite+muscovite+ feldspar+heavy mineral	8.5	52.6	16.7	xxx	14.5	24.4	xxx	xxx	16.2	11.4	27.1	14.2	xxx

Continued

Table 2. (Continued)

Parameters QFL+C QFR	Formation: sample number	Angastaco Formation								Palo Pintado Formation				
		Ans 4	Ans 5	Ans 6	Ans 9	Ans 13	Ans 14	Ans 15	Ans 17	Ans 19	Ans 22	Ans 28	Ans 30	Ans 32
Lm	Phyllite	1.1	15.8	9.7	xxx	6.5	4.7	xxx	xxx	12.3	34.2	17.1	40.4	xxx
Lm	Fine micaschist (< 32 μm)	0.0	0.0	2.8	xxx	1.6	3.5	xxx	xxx	1.1	0.0	2.9	1.4	xxx
Lm	Schist QZ+muscovite	16.0	10.5	20.8	xxx	24.2	33.7	xxx	xxx	31.8	15.2	30.0	14.9	xxx
Lm	Schist QZ+muscovite+heavy mineral	1.1	2.6	15.3	xxx	29.0	2.3	xxx	xxx	25.1	17.7	14.3	5.0	xxx
Lm	Schist QZ+epidot+chlorite+phillosilicate	0.0	0.0	0.0	xxx	0.0	0.0	xxx	xxx	0.0	0.0	0.0	0.0	xxx
Lm	Chlorite Schist	0.0	0.0	0.0	xxx	0.0	0.0	xxx	xxx	0.0	0.0	0.0	0.0	xxx
Lv	Volcanics (crystalline matrix)	43.6	0.0	13.9	xxx	0.0	0.0	xxx	xxx	1.7	8.9	0.0	2.1	xxx
Lv	Glass	0.0	0.0	0.0	xxx	0.0	0.0	xxx	xxx	0.0	0.0	0.0	0.0	xxx
Lv	Acid volcanics	0.0	0.0	1.4	xxx	0.0	0.0	xxx	xxx	0.0	0.0	0.0	0.0	xxx
Lv	Middle-basic volcanics	0.0	0.0	1.4	xxx	0.0	0.0	xxx	xxx	0.0	0.0	0.0	0.0	xxx
Lv	Pyroclastics	0.0	0.0	0.0	xxx	0.0	0.0	xxx	xxx	0.0	0.0	0.0	0.0	xxx
Ls	Argillite	0.0	0.0	0.0	xxx	0.0	0.0	xxx	xxx	0.0	0.0	0.0	0.0	xxx
Ls	Siltstone	0.0	0.0	0.0	xxx	0.0	0.0	xxx	xxx	0.0	0.0	0.0	0.0	xxx
Ls	Calcsiltstone	0.0	0.0	0.0	xxx	0.0	0.0	xxx	xxx	0.0	0.0	0.0	0.0	xxx
C	Mudstone–wackstone	0.0	0.0	0.0	xxx	0.0	0.0	xxx	xxx	0.0	0.0	0.0	0.0	xxx
C	Dolomite	0.0	0.0	0.0	xxx	0.0	0.0	xxx	xxx	0.0	0.0	0.0	0.0	xxx
C	Sparry calcite	0.0	0.0	0.0	xxx	0.0	0.0	xxx	xxx	0.0	0.0	0.0	0.0	xxx
C	Packstone-grainstone	0.0	0.0	0.0	xxx	0.0	0.0	xxx	xxx	0.0	0.0	0.0	0.0	xxx
	Total aphanitic grains	100	100	100	xxx	100	100	xxx	xxx	100	100	100	100	xxx
	Lm–Lv–Ls+C													
	Lm	49	100	82	xxx	98	100	xxx	xxx	98	91	100	98	xxx
	Lv	51	0	18	xxx	0	0	xxx	xxx	2	9	0	2	xxx
	Ls+C	0	0	0	xxx	2	0	xxx	xxx	0	0	0	0	xxx

Italic numbers in brackets correspond to altered grains of the same mineral.

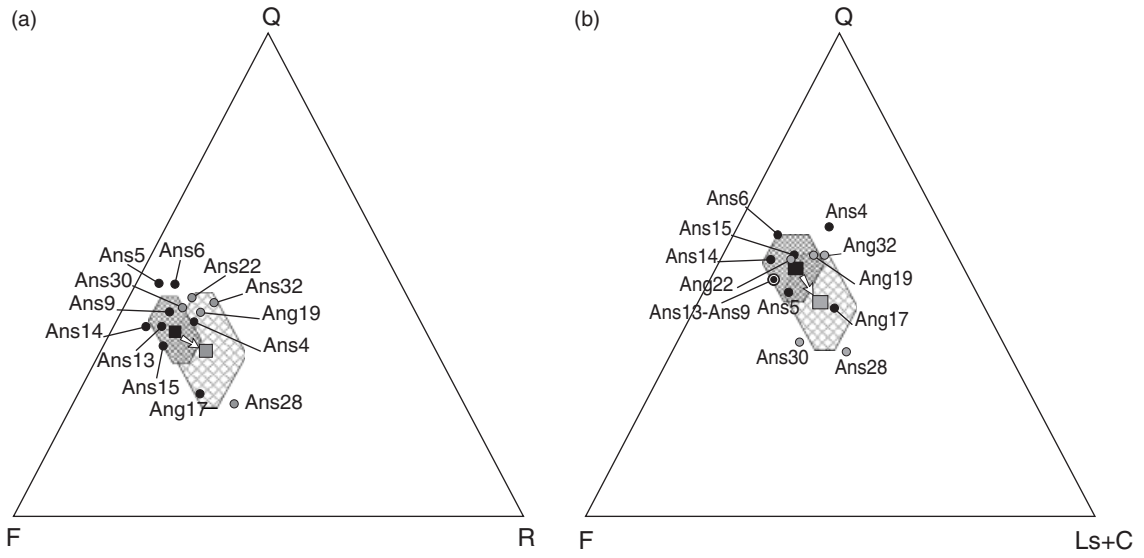

Fig. 5. Provenance discrimination diagrams. (a–c) Sandstone ternary diagrams (QFR, QFLs+C and LmLvLs+C) from point-counting analysis; raw data for the calculation of specific parameters are reported in Table 2. (d) Provenance discrimination diagram from pebble-counting analysis.

ing the parameters for the QFLs+C (G–D method) and the QFR (Folk method) diagrams, respectively (Fig. 5a and b). Additional counting of the fine lithic fraction (lithic grains with constituents $< 62\ \mu m$) was also performed (Table 2). Only nine of the 13 samples provided results and only two (Ans 20 and 32) had more than 100 fine lithics. However, a qualitative description of the lithics is provided, together with a ternary diagram (Lm–Lv–Ls+C; DiGiulio & Valloni, 1992), based on the available data (Fig. 5c). Pebble composition was also analysed in the Payogastilla Group by counting at least 100 pebbles at 25 counting stations in the field (Fig. 5d).

Results

The compositions of the Angastaco and Palo Pintado Formations are feldspathic to feldspatho-lithic, with an increasing lithic component up sequence (R, Ls+C; Fig. 5a and b). The Lm–Lv–Ls+C diagram shows an increase of metamorphic and a corresponding decrease in volcanic clasts upsection (Fig. 5c). Metamorphic lithics are mainly quartz-muscovite schist and phyllite, whereas volcanic lithics are altered and difficult to differentiate.

Clast count data reflect an up-section increase in metamorphic clasts vs. a decrease of granitic and volcanic clasts upsection; volcanics are absent from Cc 11 upward (Fig. 5d), in agreement with the sandstone petrography results. Finally, from the top of the Palo Pintado Formation and upsection, a minor (not reflected in the plots), but diagnostic contribution of red sandstone and limestone clasts of the Cretaceous Salta Group is notable. Limited published palaeocurrent data in the Angastaco and Palo Pintado Formations indicate a source in the adjacent EC to the west and northwest (Salfity *et al.*, 1984; Díaz & Miserendino Fuentes, 1988) (Fig. 1a and b).

The evidence of a source of volcanic detritus in the Puna interior is ambiguous because the volcanic lithic contents of sandstones and conglomerates are very minor or absent. However, the feldspathic to feldspatho-lithic composition of the sandstones could represent a contamination from ignimbrites that are widespread on the Puna and/or an eolian contribution by airfall tuffs (Figs 1a and 3). Occasional volcanic lithics in the basal Angastaco Formation and their eventual disappearance up-section suggest that a morphological high acting as a barrier already existed to the west-northwest of the basin in the middle Miocene, preventing volcanic material from the Puna from being fluvially transported eastward (Fig. 1a).

DETRITAL APATITE FISSION-TRACK THERMOCHRONOLOGY

Fission-track method

The majority of detrital fission-track studies to date have utilized zircon fission-track analysis because this thermochronologic system is less susceptible to post-depositional thermal overprinting (e.g. Hurford, 1986; Brandon *et al.*, 1998). However, we have used apatite crystals because in the study area, there has been too little Cenozoic exhumation to expose significant volumes of young zircons (Andriessen & Reutter, 1994; Coutand *et al.*, 2001; Deeken *et al.*, 2004).

Fission-track thermochronology is based on the spontaneous fission decay of ^{238}U in uranium-bearing minerals, which creates a linear damage zone (a fission track) in the crystal lattice. For apatite, tracks begin to be retained at temperatures below *ca.* 150–120 °C, depending on the cooling rate and the kinetic characteristics of the crystal (e.g. Green *et al.*, 1985; Ketcham *et al.*, 1999). Determining

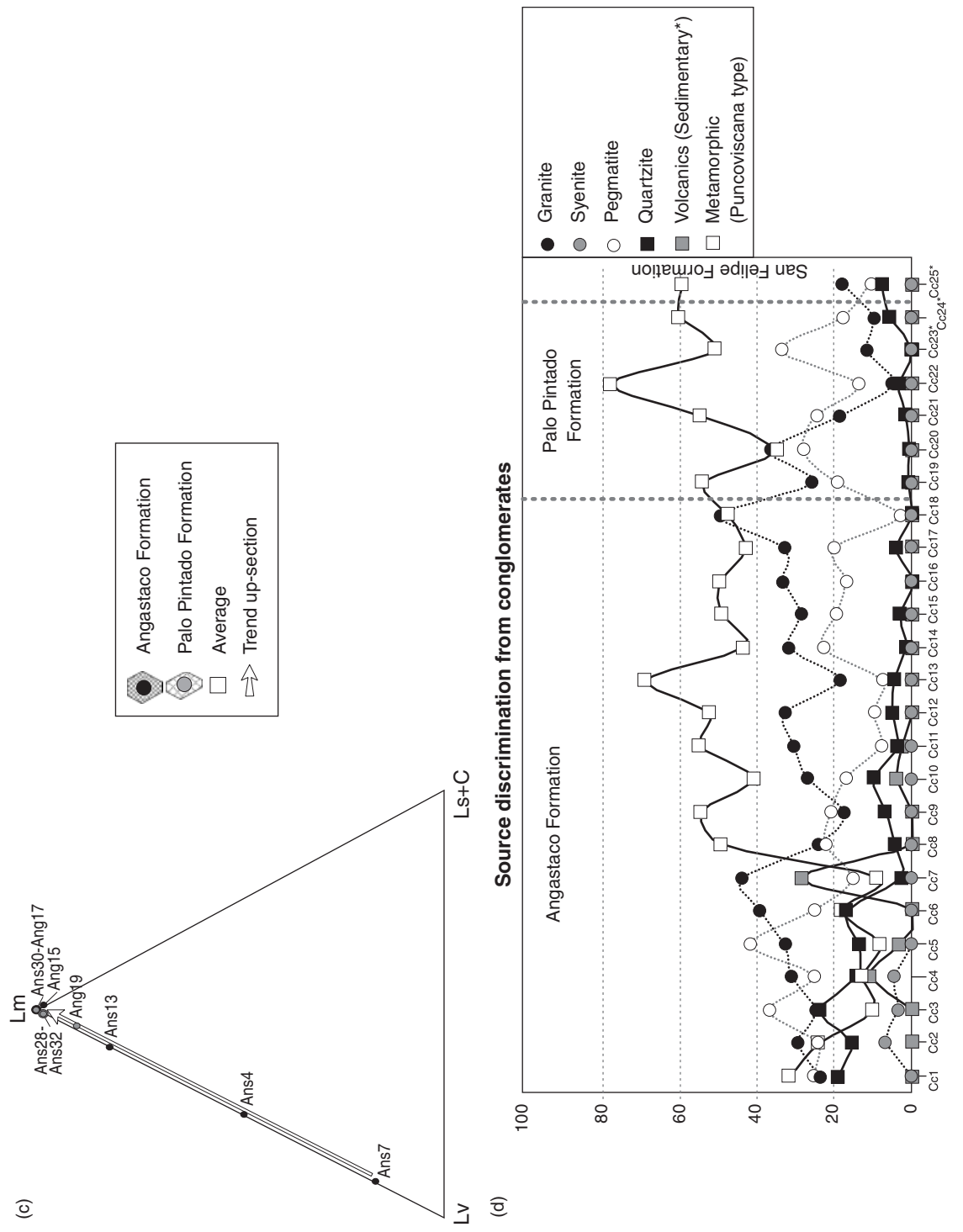

Fig. 5. Continued

the density of spontaneous fission tracks and the concentration of ^{238}U yields a single-grain fission-track age (e.g. Naeser, 1976). Fission tracks are unstable features that shorten (anneal) by thermal and time-dependent re-crystallization processes. Over geological timescales, significant track shortening occurs in fluorine-rich apatite between 60 and 110 °C (e.g. Laslett *et al.*, 1987; Laslett & Galbraith, 1996; Donelick *et al.*, 1999); this temperature range is called the partial annealing zone (PAZ) (Gleadow & Duddy, 1981; Green *et al.*, 1986). At sufficiently low temperatures, both old and new tracks are fully retained in the crystal, whereas at increasing temperatures within the PAZ, newly formed tracks are long and older tracks are progressively shortened. Therefore, a track-length distribution is a measure of the time spent within and below the PAZ.

Interpretation of a fission-track data set in terms of a *T–t* path requires an integrated analysis of fission-track age, track-length distribution and kinetic characteristics of the apatite grains. Thermal modelling programmes (Gallagher, 1995; Ketcham *et al.*, 2000) incorporate quantitative annealing models for apatite crystals with different kinetic characteristics (Laslett *et al.*, 1987; Ketcham *et al.*, 1999).

Twelve sandstone samples, ~6–10 kg in weight, were collected through the continuous ~6200-m-thick Angastaco section, with an average sample spacing of ~600 m (Table 3, Fig. 3). In the laboratory, bulk samples were crushed, washed, sieved and apatite crystals were separated using standard magnetic and heavy liquids methods. Analytical details are presented in Table 3. About 100 grains were dated per detrital sample (Tables 3 and 4). For each sample, fission-track grain-age (FTGA) distributions were decomposed following the binomial peak-fit method (Galbraith & Green, 1990) incorporated into BINOMFIT program (Brandon, 1992, 1996; for details see, Brandon, 2002) to identify discrete populations (or components, P_1 to P_n). The ages within each component are by definition concordant. Confined track lengths were only measured in crystals that were dated; the angles between the confined track and the *C*-crystallographic axis (*C*-axis projected data) and the etch pit diameter (D_{par}; Donelick *et al.*, 1999) were also measured.

Results

The FTGA distributions typically show a large single-grain age span, from 166 to 2 Ma (Fig. 6), with central ages ranging between 62.6 ± 2.4 and 28.9 ± 2.5 Ma (Table 3). All samples clearly fail the χ^2 test (Galbraith, 1981; Green, 1981) with $P(\chi^2) = 0$ (Table 3), indicating that FTGA distributions are discordant and are a mixture of components or peak ages (Brandon, 1992, 1996). All observed FTGA distributions were decomposed into their main grain-age components or peaks and yielded three to five components per sample (P_1, . . . , P_n from the youngest to the oldest peak, Table 4). Assignment of each FTGA component to a detrital D_n path (Ruiz *et al.*, 2004) or trend and consequent interpretations are presented below.

Confined track-lengths and D_{par} measurements were obtained from the greatest possible number of dated grains. Using BINOMFIT, each singular dated grain, track length and D_{par} measurement was assigned to a specific peak age. Thus, we obtained representative track-length distributions for 14 peak ages (number of tracks > 20 except in three cases), mainly from P_4 and P_5 (for details, see Table 5), as expected from their older apparent ages, and hence higher fission-track density. The mean track lengths did not vary significantly throughout the sedimentary section (Table 5, Fig. 7); values ranged between 11.55 ± 0.31 and 12.93 ± 0.26 μm. There was no clear trend in the mean track-length vs. stratigraphic position (Fig. 7). All populations yielded similar D_{par} values of 1.64–1.94 μm (Table 5), suggesting that all populations contained monocompositional apatites with similar low resistance to annealing.

EVIDENCE AGAINST THERMAL RESETTING

The interpretation of detrital apatite FT ages depends on whether the ages have been partially reset by post-depositional burial and reheating. We are particularly concerned about this problem because of the large thickness of the sampled sedimentary sequence (> 6000 m). However, for the following reasons, our observations argue strongly against significant post-depositional annealing:

(1) All the FTGA distributions are discordant; even with multiple ages, there could still be a possibility that less retentive grains have been selectively reset and give younger peak ages (Garver *et al.*, 1999). However, all populations have apatites with similar kinetic characteristics (Table 5), ruling out this possibility. (2) All resolvable peak ages in the distributions are older than the depositional age (Table 4); furthermore, very young age peak recurrently appear close to the depositional age but never younger than it. (3) Both the central ages and the peak ages increase systematically down-section, whereas partially annealed samples would show the opposite (Tables 3 and 4). (4) Finally, progressive burial heating should be expressed as a decrease in the mean track-length with depth; however, such a variation was absent (Table 5 and Fig. 7). These observations indicate that the detrital grain ages reflect cooling in the source area because partial annealing due to burial reheating during the sedimentary filling of the Angastaco basin did not occur as intensely as expected for such a thick preserved sedimentary section. Two possible explanations for this unanticipated result include: (1) the effective geothermal gradient in the basin was reduced because of the effects of rapid sedimentation and topographically driven groundwater recharge (Garven, 1989; Deming *et al.*, 1990; Willett *et al.*, 1997); and (2) complex structural and depositional geometries lead to depocentre migration, preventing the base of the section from being buried beneath the full stratigraphic thickness. Below, we explore both of these possibilities.

Table 3. Apatite fission track data from Angastaco basin

Sample	Location		Stratigraphic unit	Cumulative thickness (m)	Number of grains (N)	Spontaneous $\rho_s \times 10^6\,cm^{-2}$ (N_s)	Induced $\rho_i \times 10^6\,cm^{-2}$ (N_i)	Dosimeter $\rho_d \times 10^6\,cm^{-2}$ (N_d)	$P(\chi^2)$ (%)	Central age $\pm 1\sigma$ (Ma)
	Latitude (°S)	Longitude (°W)								
AI1	25°41.584	66°10.067′	Angastaco Fm.	0	96	1.0114 (5456)	3.0767 (16 598)	1.0843 (5261)	0	62.6 ± 2.4
AI6	25°41.104	66°09.135′	Angastaco Fm.	601.7	110	1.1698 (7165)	4.1051 (25 144)	1.0932 (5261)	0	56.7 ± 2.7
AI9	25°41.409	66°08.686′	Angastaco Fm.	1066.4	91	0.8359 (3636)	2.8289 (12 305)	1.1022 (5261)	0	59.6 ± 2.5
AI11	25°41.440′	66°08.178′	Angastaco Fm.	1620.3	100	0.7919 (5623)	2.7905 (19 813)	1.1111 (5261)	0	53.9 ± 2.3
AI13	25°41.960′	66°07.697′	Angastaco Fm.	2235.9	48	0.5577 (1653)	2.2674 (6720)	1.1179 (5261)	0	47.2 ± 3.0
AI16	25°42.780′	66°07.519′	Angastaco Fm.	3280.3	115	0.9432 (8542)	3.1059 (28 128)	1.1335 (5261)	0	59.4 ± 2.4
AI18	25°41.282′	66°06.261′	Angastaco Fm.	3945.5	100	0.6655 (3413)	2.5634 (13 146)	1.1447 (5261)	0	52.4 ± 2.6
AI23	25°40.440′	66°05.507′	Palo Pintado Fm.	4578.5	104	0.9746 (7015)	3.6268 (26 104)	1.2604 (9321)	0	45.9 ± 3.6
AI25	25°40.603′	66°04.979′	Palo Pintado Fm.	5077.3	97	0.6729 (3175)	3.708 (17 496)	1.2869 (9321)	0	43.1 ± 2.4
AI26	25°40.313′	66°04.654′	Palo Pintado Fm.	5508.5	101	0.5617 (3331)	3.5825 (21 246)	1.3134 (9321)	0	38.4 ± 2.7
AI28	25°40.412′	66°04.334′	Palo Pintado Fm.	6027.1	100	0.4183 (2697)	2.9695 (19 146)	1.3399 (9321)	0	28.9 ± 2.5
AI35	25°40.432′	66°02.214′	San Felipe Fm.	xxx	100	0.6567 (4691)	3.0718 (21 943)	1.3664 (9321)	0	48.4 ± 2.8

Notes: Cumulative stratigraphic thickness is measured from the bottom of the Angastaco Fm. to the top of the Palo Pintado Fm.; N, number of individual grains dated per sample; ρ_s, spontaneous track density; N_s, number of spontaneous tracks counted; ρ_i, induced track density in external detector (muscovite); N_i, number of induced tracks counted; ρ_d, induced track density in external detector adjacent to dosimetry glass; N_d, number of tracks counted in determining ρ_d; $P(\chi^2)$, χ^2 probability; Trackkey software (Dunkl, 2002) was used for calculating the central fission track ages $\pm 1\sigma$. Apatite aliquots were mounted in araldite epoxy on glass slides, ground and polished to expose internal grain surfaces, then etched for 20 s in 5.5 M HNO_3 at 21 °C to reveal spontaneous fission tracks. All mounts were prepared using the external-detector method (Hurford & Green, 1983). Samples and CN-5 glass standards were irradiated with thermal neutrons in the well-thermalized Oregon State University reactor. After the irradiation, the low-U muscovite detectors that covered apatite grain mounts and glass dosimeter were etched in 40% HF for 45 min at 21 °C to reveal induced fission tracks. Samples were analysed with an Olympus BX61 microscope at × 1250 magnification with a drawing tube located above a digitizing tablet and a Kinetek computer-controlled stage driven by the FTStage programme (Dumitru, 1993). Fission-track ages were calculated using a weighted mean zeta calibration factor (Hurford & Green, 1983) based on IUGS age standards (Durango, Fish Canyon and Mount Dromedary apatites) (Miller *et al.*, 1985, Hurford, 1990). Based on 19 analyses, the ζvalue for *I.* Coutand is 369.6 ± 5.1 (± 1 standard error).

Table 4. Best-fit age populations for apatite FTGA samples from the Angastaco basin

Sample	Stratigraphic age (Ma)	N	FTage range (Ma)	P_1	P_2	P_3	P_4	P_5	P_6
AI 35	[3.4–1.6]	100	3.9–118.7	xxx	12.7 ± 2.6/2.1 *20.1%*	xxx	xxx	50 ± 3.3/3.1 *56.4%*	82.7 ± 7.0/6.4 *23.5%*
AI 28	5.6	100	2.6–110.9	6.6 ± 1.4/1.2 *39.1%*	xxx	22.5 ± 2.9/2.6 *20.3%*	xxx	60.9 ± 3.8/3.6 *40.6%*	xxx
AI 26	6.5	101	4.0–139.7	xxx	14.3 ± 1.5/1.3 *41.3%*	xxx	xxx	53.2 ± 3.5/3.3 *51.9%*	103.9 ± 20.6/17.2 *6.9%*
AI25	7.3	97	3.8–100.5	xxx	xxx	20.6 ± 3.2/2.8 *32.8%*	45.6 ± 20.5/14.1 *44.0%*	75.7 ± 20.0/15.9 *23.2%*	xxx
AI23	8.3	104	3.9–154.3	9.9 ± 1.5/1.3 *40.5%*	xxx	xxx	xxx	70.8 ± 6.1/5.7 *52.6%*	123.2 ± 56.1/38.6 *6.9%*
AI18	9.3	100	5.9–166.6	xxx	17.7 ± 5.9/4.4 *7.5%*	xxx	39.8 ± 4.0/3.7 *41.2%*	67.3 ± 4.7/4.4 *48.9%*	158.2 ± 48.4/37.2 *2.4%*
AI16	10.1	115	3.0–156.5	10.2 ± 12.8/5.7 *5.8%*	xxx	26.8 ± 13.1/8.8 *6.3%*	56 ± 4.6/4.3 *45.1%*	74 ± 5.4/5.1 *39.8%*	119.7 ± 35.1/27.2 *3%*
AI13	11.4	48	14.3–102.3	xxx	xxx	31.3 ± 5.3/4.5 *39.9%*	51.8 ± 7.1/6.3 *46.5%*	84.7 ± 12.6/11.0 *13.6%*	xxx
AI11	12.2	100	13.8–133.8	15.6 ± 8.0/5.3 *3.6%*	xxx	36.6 ± 4.2/3.8 *33.0%*	60.9 ± 3.9/3.7 *48.9%*	82.2 ± 8.6/7.8 *13.5%*	128.5 ± 91.3/53.6 *0.9%*
AI9	12.9	91	21.0–158.8	xxx	xxx	30.2 ± 6.9/5.6 *10.4%*	49.1 ± 5.4/4.9 *39.5%*	75.5 ± 5.6/5.2 *50.2%*	xxx
AI6	13.5	110	11.4–129.1	14.3 ± 2.0/1.8 *12.4%*	xxx	36.7 ± 4.5/4.0 *16.7%*	65.3 ± 4.6/4.3 *54.0%*	88.4 ± 12.2/10.7 *16.9%*	xxx
AI1	14.3	96	15.4–147.0	xxx	xxx	40.2 ± 4.3/3.9 *30%*	72.1 ± 3.9/3.7 *68.7%*	xxx	130 ± 34.2/27.1 *1.2%*

Notes: Binomial peak-fit ages (P_1–P_6) were determined with BINOMFIT (Brandon, 1996; 2002) and are indicated by their mean age ± 2 SE (equivalent to 95% confidence interval; note that these intervals are asymmetric), followed by their relative abundance (%); N, total of grains counted.
FTGA, fission-track grain age.

In a basin that is in a thermal steady state, the basal temperature is given by

$$T = \mathrm{sum}(z_i(Q/k_i)) + T_0 \quad (1)$$

where Q is the heat flow ($\mathrm{mW\,m^{-2}}$), k_i is the thermal conductivity of a lithologic unit ($\mathrm{W\,m^{-1}\,K^{-1}}$), z_i is the thickness of that unit and T_0 is the mean surface temperature, taken to be 10–15 °C.

Heat flow data are not available in the study area; however, an extensive study in Bolivia provides predictions for different tectonic elements within the Central Andes (Springer & Förster, 1998), suggesting that the heat flow in the EC is between 60 and 40 $\mathrm{mW\,m^{-2}}$. Thermal conductivity data are not available. Therefore, we consider a range of plausible conductivities based on the literature values (e.g. Blackwell & Steele, 1988). We subdivided the Angastaco basin section into three units from bottom to top: sandstone (4200 m), shale with subordinate sandstone (1500 m) and sandstone (1100 m). For these three units, we examined thermal conductivities of 2.0–3.0, 1.4–2.3 and 2.0–3.0 $\mathrm{W\,m^{-1}\,K^{-1}}$, respectively. At steady state, these parameters implied basal temperatures between 107 and 238 °C, far in excess of the maximum temperature required to preserve the observed detrital thermochronometric signal. This suggests that the Angastaco basin did not reach a thermal steady state.

Transient effects associated with rapid sedimentation can depress the geothermal gradient in a sedimentary basin (e.g. Deming *et al.*, 1990). In the Angastaco basin, accumulation rates were 700 ± 100 $\mathrm{m\,Ma^{-1}}$, which is rapid. Such transient effects could allow for a slightly thicker effective burial depth. Topographically driven groundwater recharge may also affect the thermal structure of a basin, cooling proximal areas and heating more distal regions (Garven, 1989; Willett *et al.*, 1997). This effect could perhaps explain 10–20 °C of cooling; however, hydraulic data required to quantitatively test this hypothesis are lacking.

The stratal geometry in the Angastaco basin is poorly constrained by field observations because of lack of 3-D exposure. However, the overall structural style of an eastward-migrating deformation front observed in this area favours syntectonic growth strata. In particular, in the absence of an eastward migration of the depocentre, both the subsidence and the exhumation rate of the basin would be extremely high. Therefore, it is plausible that depocentre migration prevented the sampled base of the section from having been buried beneath the 6-km-thick section.

Although we cannot definitively prove which of these explanations is more important, both arguments are con-

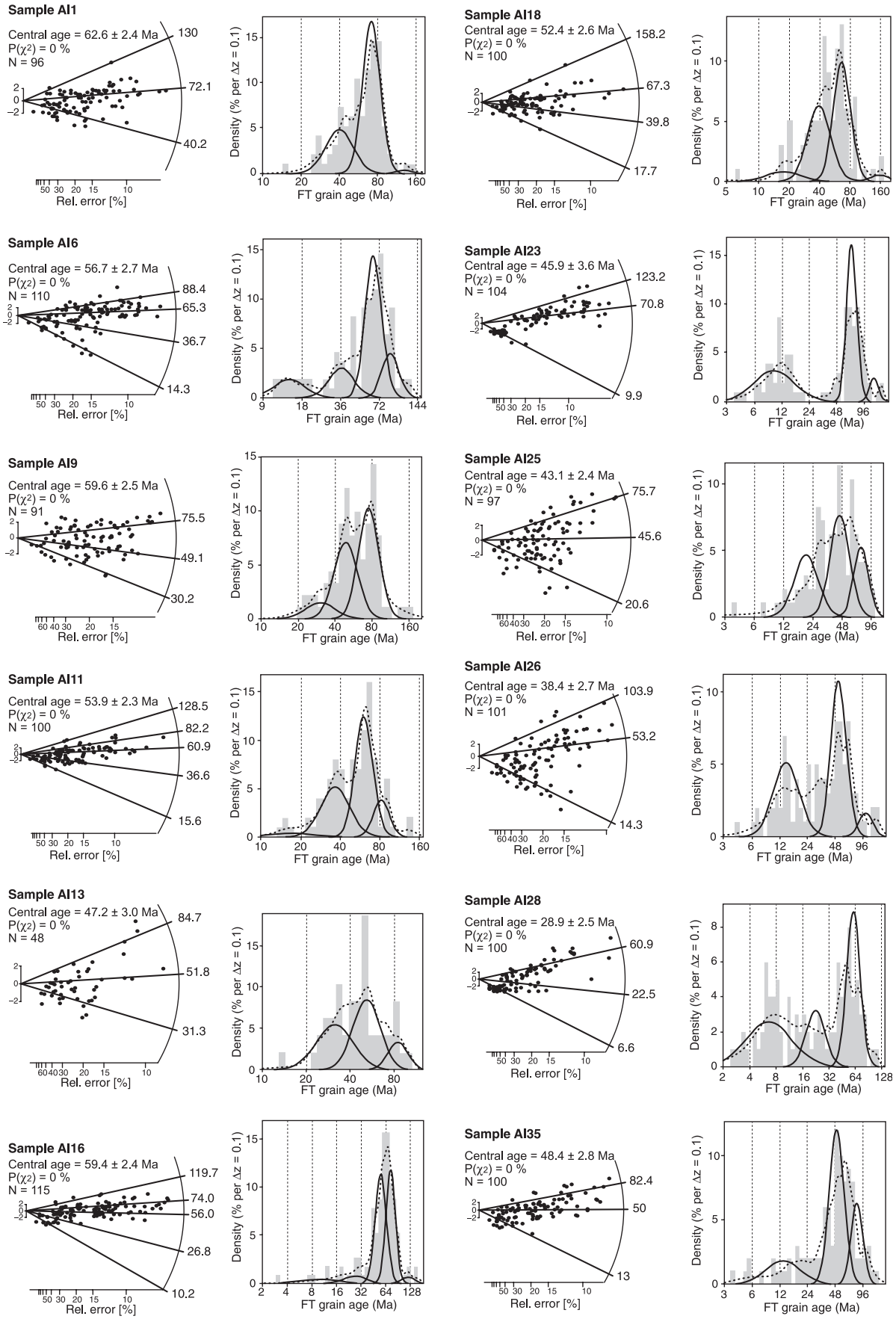

Fig. 6. Detrital apatite fission-track results. Radial plots of the single-grain age data and probability density plots of fission-track grain-age distributions (Brandon, 1996). Dashed lines indicate probability density distributions and solid lines indicate component distributions estimated by the binomial peak-fit method (Galbraith & Green, 1990).

Table 5. Mean-track length and related etch pit (D_{par}) values obtained for different detrital age components

Sample	Component	Peak age (± 95% CI) (Ma)	Number of tracks	Mean track length (μm ± 1σ)	Mean track length STD (μm)	D_{par} (μm)	D_{par} STD (μm)
AI1	P_4	72.1 ± 3.9/3.7	78	12.3 ± 0.17	1.46	1.71	0.12
AI6	P_3	36.7 ± 4.5/4.0	13	12.2 ± 0.32	1.16	1.74	0.07
	P_4	65.3 ± 4.3/4.6	61	12.44 ± 0.15	1.25	1.70	0.09
	P_5	88.4 ± 12.2/10.7	30	11.73 ± 0.31	1.69	1.75	0.17
AI9	P_5	75.5 ± 5.6/5.2	33	11.72 ± 0.27	1.55	1.71	0.12
AI11	P_4	60.9 ± 3.9/3.7	22	11.55 ± 0.31	1.45	1.69	0.15
	P_5	82.2 ± 7.8/8.6	21	11.76 ± 0.40	1.83	1.71	0.10
AI16	P_4	56.0 ± 4.6/4.3	28	12.53 ± 0.19	0.99	1.67	0.08
	P_5	74.0 ± 5.4/5.1	75	11.83 ± 0.18	1.60	1.64	0.09
AI18	P_4	39.8 ± 4.0/3.7	20	12.88 ± 0.28	1.26	1.94	0.42
	P_5	67.3 ± 4.7/4.4	22	12.07 ± 0.32	1.49	1.78	0.19
AI23	P_5	70.8 ± 6.1/5.7	57	12.0 ± 0.16	1.20	1.75	0.19
AI25	P_5	75.7 ± 20.0/15.9	19	12.07 ± 0.19	0.81	1.85	0.10
AI26	P_5	53.2 ± 3.5/3.3	22	11.71 ± 0.40	1.88	1.72	0.15
	P_6	103.9 ± 20.6/17.2	17	12.12 ± 0.41	1.68	1.92	0.14
AI28	P_5	60.9 ± 3.8/3.6	43	12.93 ± 0.26	1.68	1.75	0.16
AI35	P_5	50.0 ± 3.3/3.1	24	12.62 ± 0.36	1.76	1.79	0.19
	P_6	82.7 ± 7.0/6.4	33	11.77 ± 0.32	1.82	1.79	0.12

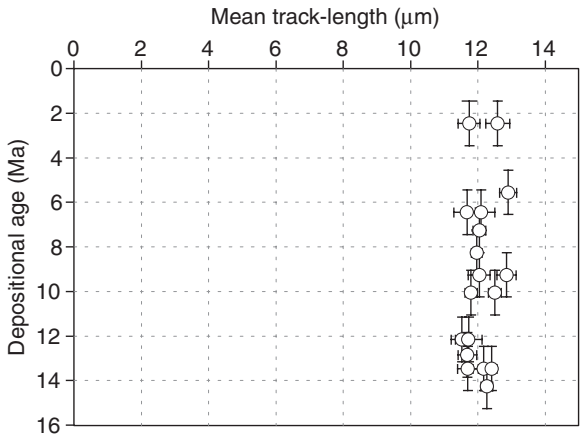

Fig. 7. Mean track-length values plotted against depositional age (see also Table 5).

sistent with the basic observation that the AFT data were not significantly reset by burial during filling of the basin. Hence, our data most likely reflect the thermal history of the source terrains of the clastic material.

DETRITAL THERMOCHRONOLOGY AND HINTERLAND EVOLUTION

The distribution of detrital mineral cooling ages in sediments can provide a record of the erosional exhumation of the hinterland source area. However, converting a cooling age extracted from a detrital sample into an exhumation rate for the source area requires several major assumptions that we briefly discuss below (for a review, see Garver *et al.*, 1999; Brewer *et al.*, 2003; Ruiz *et al.*, 2004).

The procedure used to derive the average exhumation rate of a hinterland source from a population of thermochronologic data collected through a reasonably well-dated sedimentary sequence is discussed by Garver *et al.* (1999). In summary, the average exhumation rate is given by

$$\mathrm{d}z/\mathrm{d}t = ((T_c - T_s)/(\mathrm{d}T/\mathrm{d}z))/\Delta t \quad (2)$$

which is equivalent to

$$\mathrm{d}z/\mathrm{d}t = Z_c/\Delta t \quad (3)$$

where T_c is the closure temperature of the thermochronometer, T_s is the surface temperature, $\mathrm{d}T/\mathrm{d}z$ is the geothermal gradient, Δt is the lag time and Z_c is the closure depth. The lag time is defined as the time elapsed between the time of closure of a crystal for a given geochronological system in the source region and the time at which it is deposited in the sedimentary basin. The assumption is usually made that the time taken by newly eroded detritus to be transported and then deposited in the sedimentary basin is negligible compared with the time taken to reach the surface (and be eroded) from the closure depth (Cerveny *et al.*, 1988; Garver *et al.*, 1999; Ruiz *et al.*, 2004). Thus, to be valid, the lag time concept implies that during their transit from the source to the basin, the detritus are not stored in transient depocentres during time periods long enough (*ca.* $\geq$ 1 Ma) to bias their stratigraphic age in the basin significantly. In addition, subsequent to deposition, recycling of non-reset sediments does not significantly modify the initial stratigraphic age (Ruiz *et al.*, 2004). Perhaps the most significant condition for the Angastaco basin is that the detritus must have cooled from a temperature higher than the apatite fission-track T_c. If this

were not the case, detrital thermochronologic data collected could not be converted into exhumation rates for the corresponding source regions.

For hinterland regions, our approach requires other assumptions. It is necessary to assume a steady geothermal gradient at the time of closure of the geochronological system, although the geothermal gradient at that time is not trivial to derive (Garver *et al*., 1999). Isotherms are assumed to remain horizontal and particle paths toward the surface vertical. The exhumation rate remains constant from the time of closure to the time of deposition of the crystal. Hence, this approach neglects isotherm warping in the source region caused by topography and advection (e.g. Stüwe *et al*., 1994; Mancktelow & Grasemann, 1997; Braun, 2002) as well as non-vertical displacements of particles during exhumation (Batt & Brandon, 2002). As long as the spatial distribution of cooling ages within a source catchment during a time increment remains difficult to determine (Brewer *et al*., 2003), quantifying exhumation rates from detrital thermochronologic data is fraught with uncertainty. Finally, the simplest model supposes that the exhuming topography is eroded principally from higher elevations and strictly in a vertical direction. In reality, the drainage basin may cover a large range of elevations in the source topography; thus, different peak ages identified in the detrital sediments will not necessarily be derived from distinct source terrains but rather could be derived from different elevations within a single catchment (Garver *et al*., 1999). These restrictions imply that interpretation of detrital peak age provenance as well as long-term exhumation rates derived from them should always be treated with caution. Nevertheless, detrital thermochronology remains a valuable tool for constraining the cooling and exhumation history of sources terrains partially or totally eroded.

INTERPRETATION OF THE ANGASTACO BASIN DETRITAL SIGNAL

Plotting the fission-track ages of a given component vs. the stratigraphic ages of the host strata yields a graphical assessment of the lag time variability through the stratigraphic column and thus, through time (e.g. Ruiz *et al*., 2004), thereby providing information on the long-term exhumation of the source region for that particular detrital age population (Fig. 8). The source-area signal of the proximal Angastaco foreland basin changes through time, for instance because of sporadic drainage re-organization, and unlike Ruiz *et al*. (2004), we do not expect every sample to contain the same number of P_n age components. Consequently, our D_n paths or trends are not defined by automatically connecting individual components with the same n of each sample. Instead, we sorted the P_n components such as they defined geologically realistic processes smoothly evolving through time following a D_n trend.

Here, we describe this population subdivision and subsequently interpret each path. In this dataset, lag time for each path either remains constant or decreases upsection, which is consistent with exhumation. Increasing lag times could represent recycling of sediments. Although we cannot exclude such a process, if it exists, the resulting signal appears to be hidden behind the dominant decreasing lag time trend.

P_1 component

The first population (P_1) had extremely short lag times (Fig. 8 and Table 4); five samples had cooling ages between 15.6 and 6.6 Ma and lag times between 0 and 4 Ma.

A constant lag time approaching 0 reflects either persistent and extremely rapid cooling and exhumation in the hinterland or volcanic contamination of the clastic material shed into the basin (Ruiz *et al*., 2004). The published apatite fission-track data set in the Andean hinterland at these latitudes (e.g. Andriessen & Reutter, 1994; Coutand *et al*., 2001; Deeken *et al*., 2004; Carrapa *et al*., 2005) does not reveal any ages young enough to produce the detrital ages in population P_1, suggesting that rapid exhumation was not the cause of this young age component. Alternatively, the hypothesis of volcanic contamination seems plausible. The region contains numerous airfall tuffs with similar ages (Strecker *et al*., 1989; Grier & Dallmeyer, 1990; Muruaga, 2001a, b) (Fig. 3). The P_1 population is present from bottom to top of the stratigraphic section but sporadically, as would be expected from episodic input of volcanic ash into the basin.

P_2 component

The next population, P_2, contains only three samples with ages between 17.7 and 12.7 Ma, and similar lag times of 8–10 Myr. It first appears at 9.3 Ma; however, it is possible that the next older sample ($\sim$10 Ma) contains some grains with similar ages that have not been statistically distinguished from the P_1 population.

The relatively constant lag time of 8–10 Ma is characteristic for a constant, high erosion rate (Bernet *et al*., 2001; Ruiz *et al*., 2004) and likely representative of material that has rapidly cooled through the entire apatite PAZ. For a lagtime $\Delta t = 8$–10 Myr, $T_c = 110 \pm 5\,^{\circ}\mathrm{C}$, $T_s = 15\,^{\circ}\mathrm{C}$, $\mathrm{d}T/\mathrm{d}z = 25 \pm 5\,^{\circ}\mathrm{C\,km^{-1}}$, Eqn (2) yields a range of exhumation rates of 0.3–0.6 mm yr^{-1}. This signal first appears at 9–10 Ma, suggesting that at this time either the first apatites exhumed from below T_c were exposed at the surface or that drainage reorganization, which first supplied this detritus to the basin, had occurred. One method to differentiate between these possibilities is to ascertain whether apatites representing the exhumed PAZ are preserved in the basin; this is discussed below (see P_4). Alternatively, we can look for appropriate source areas in the vicinity of the basin. Palaeocurrent directions throughout the section suggest sediment transport from the west (e.g. Starck & Anzótegui, 2001). The Cumbres de Luracatao, belonging to the EC (Figs la and 2a), is the most prominent range to the west of the Angastaco basin and contains granite and granodiorite of the Oire intrusive complex. Three AFT vertical profiles from the northern portion of this range

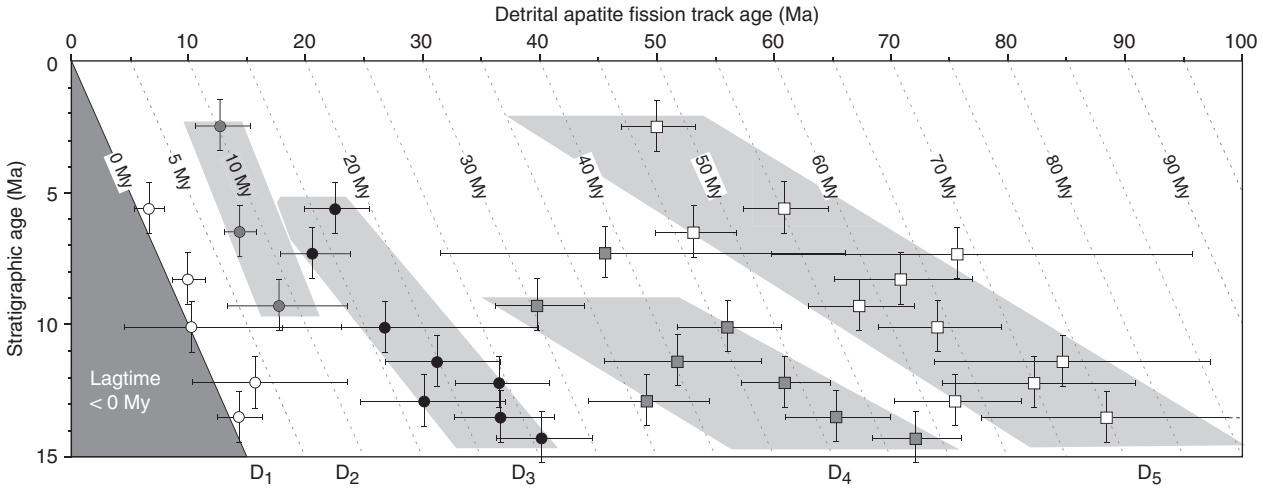

Fig. 8. Evolution of the detrital paths (D_1–D_5) through the stratigraphic record. Error bars are $\pm$ 2 SE for apatite FT ages and $\pm$ 1 Ma uncertainty for depositional ages. Dashed grey lines indicate iso-lag time lines. Symbols indicate binomial peak-fit ages extracted from the mixed grain age distributions (P_1–P_6, see Table 4 and Fig. 6) and grey shaded boxes underline related detrital path tendency upsection (D_1–D_5).

reveal reset AFT ages between 16 and 20 Ma over a combined elevation range of 2100 m (Deeken *et al.*, 2004). A single partially reset sample at high elevation defines a kink in the age–elevation curve and suggests that relatively rapid exhumation commenced by 20 Ma at *ca.* 0.4 mm yr^{-1}. At this exhumation rate, the first reset apatites would have been exposed at the surface at *ca.* 10 Ma. The similar age range and exhumation rate observed at Cumbres de Luracatao and in the D_2 trend suggests a genetic link. However, the youngest ages observed in the D_2 path have not yet been retrieved from bedrock samples.

P_3 component

The third component (P_3) had cooling ages between 40.2 and 20.6 Ma; D_3 path is a 'forward-moving peak' with a lag time that regularly decreases upsection from ~25 Myr at the bottom to ~15 Myr at the top (Fig. 8). This kind of pattern is generally interpreted as reflecting an overall increase in cooling rate in the source region through time and is classically interpreted as being associated with a phase of orogenic growth (Garver *et al.*, 1999). However, this statement is valid only if the ages recorded by the apatite crystals reflect cooling through the closure temperature. For young, non-volcanic apatites, this hypothesis is likely correct; for older apatites with very long lag times, and hence very slow cooling rates, this is probably incorrect. In the case that the samples were fully reset during the ultimate exhumation event, an exhumation rate can be calculated using the same approach as was applied for P_2, resulting in 0.1–0.2 mm yr^{-1} at the base and increasing to 0.2–0.3 mm yr^{-1} at 5 Ma. The lowest sample in the P_3 population reflects cooling during the interval from 40 Ma (passing through T_c) to 14.3 Ma (deposition in the basin); the youngest sample in P_3 reflects cooling between 21 and 7.3 Ma. Potential source areas with similar ages (e.g. 38 $\pm$ 3 to 29 $\pm$ 3 Ma) have been dated in the Chango Real Range, located *ca.* 100 km to the SSW (Fig. la and b) (Coutand *et al.*, 2001) and a single age of 30.3 $\pm$ 3.0 has been reported from Santa Rosa de Tastil (Quebrada del Toro) located *ca.* 100 km to the NNE (Fig. la and b) (Andriessen & Reutter, 1994). Both localities are part of the present-day EC. Although neither of these ages provides an exact match to the P_3 component, they suggest that appropriate sources existed on the eastern flank of the Andes. Cooling ages of 29 $\pm$ 1 to 24 $\pm$ 3 Ma have been obtained from Sierra de Calalaste, in the southern Puna plateau to the west (Carrapa *et al.*, 2005). A large suite of AFT data with ages between 62 and 30 Ma characterizes the Cordillera Domeyko in the Western Cordillera (Chile) (Maksaev & Zentilli, 1999). However, the scarcity of volcanic material within the Angastaco basin, which would be expected from fluvial systems draining the Puna, strongly argues against source areas on the far western side of the plateau. Although it has not yet been precisely identified in the modern landscape, the source for the P_3 component must be located within the present-day EC

P_4 component

The fourth population, P_4, contains a much broader range of cooling ages and a less well-defined trend on the lag time plot. Cooling ages range between 65.3 and 39.8 Ma; this population disappears from the section above *ca.* 7 Ma. D_4 is also a 'forward-moving peak'; however, the lag time decreases upsection in a complicated pattern, from ~57 Myr at the bottom to ~30 Myr at 9 Ma (Fig. 8). The stratigraphically youngest FTGA peak has a longer lag time of 38 Myr and an age of 45 $\pm$ 21/14 Ma (sample AI25, see Table 4 and Fig. 8). The next older FTGA peak in this sample also has a very large error bar; the errors of these two age clusters overlap. Therefore, we suspect that the peak ages for this sample are poorly resolved and we do not consider them to be highly significant. More importantly, no FTGA peaks for P_4 are identified higher in the stratigraphic section (Fig. 8). This suggests two possibili-

ties: (1) the component representing this source area was no longer deposited in the basin after *ca*. 9 Ma, or (2) the D_4 path became significantly younger at this time. The former idea cannot be ruled out: similar ages are present in the Sierra Famatina *ca*. 350 km to the south (Coughlin *et al*., 1998). However, 9 Ma corresponds closely to the first appearance of the P_2 component. Therefore, it is possible that the D_4 path represents the exhumed PAZ that formerly overlay the P_2 source area. We link the latter source area with rapid exhumation of Cumbres de Luracatao, commencing at *ca*. 20 Ma. A single sample from the exhumed PAZ that formerly overlay the range yielded an age of 56 ± 2 Ma (Deeken *et al*., 2004), fitting well with the age range recorded by P_4. The large scatter of ages within the D_4 path is consistent with the exhumation of a PAZ, because a variety of ages would be exposed within a narrow range of elevation. The pronounced decrease in age upsection in D_4 is also more typical of exhumation through a PAZ. Therefore, we conclude that the proximal Cumbres de Luracatao is a likely source for the P_4 component.

P_5 component

The fifth component (P_5) has cooling ages between 88.4 and 50.0 Ma. P_4 and P_5 together contribute between 50 and 70% of the dated crystals (Table 4). D_5 is a 'forward-moving peak' with ages and lag times decreasing upward from 88 to 50 Ma and 75 to 47 Myr, respectively. Indeed, the rigorous definition of a lag time applies to neither these samples nor the P_4 component; the old ages and extremely long lag times suggest that this material was derived from an exhumed PAZ that was slowly eroded rather than cooled through a closure temperature T_c. A vertical AFT profile through Cerro Durazno, immediately west (Fig. 2a), yielded cooling ages between 95 and 52 Ma (Deeken *et al*., 2004; A. Deeken, E.R. Sobel, I. Coutand, M. Haschke, U. Riller & M.R. Strecker, submitted). Track-length modelling of these samples indicates exhumation commencing between 12 and 7 Ma (A. Deeken, E.R. Sobel, I. Coutand, M. Haschke, U. Riller & M.R. Strecker, submitted). Similar ages between 93 ± 5 and 42 ± 2 Ma were reported from Santa Rosa de Tastil at 24°S (Coutand, 1999). The similarity likely reflects a common tectonothermal history; however, the detritus in the basin was most likely derived from the adjacent Durazno range. The similar age range of the P_5 component and the adjacent Cerro Durazno suggests that they represent the same (late) Cretaceous PAZ.

P_6 component

The oldest population (P_6) ranges between 158.2 and 82.7 Ma, with lag times between 150 and 80 Myr. Most of these FTGA peaks represent a minor fraction of the dated crystals (1–7%) and hence have quite large errors; however, the youngest sample AI35 contains 23% of the detrital apatite (Table 4). There is a crude decrease in age and lag time upsection (not represented in Fig. 8); however, with the exception of the stratigraphically youngest sample, this pattern is poorly resolved. There are several potential sources for this minor component. One possibility is the Puna plateau, which includes old AFT source regions (Deeken *et al*., 2004; A. Deeken, E.R. Sobel, I. Coutand, M. Haschke, U. Riller & M.R. Strecker, submitted), but our sedimentary petrography data argue against this. Alternatively, the presently outcropping Cretaceous and Palaeogene strata could have provided a source for recycled detrital apatite with old ages.

DISCUSSION

Sandstone petrography and clast counts in conglomerates identify the EC as the main source of the detritus deposited in the intramontane Angastaco basin between 14.5 and 5.5 Ma. A cooling event starting in the late Eocene–Oligocene is clearly visible in the D_3 detrital path. This source was exhumed until the Pliocene at a rate increasing from 0.1 to 0.3 mm yr^{-1}. Although the location of the source area has not yet been identified, the existence of modern outcrops that yielded late Eocene to Oligocene rapid cooling AFT ages (Andriessen & Reutter, 1994; Coutand *et al*., 2001) supports a provenance from the EC. We propose that this cooling event reflects an early compressional episode in the eastern part of the Andean orogen. This event created enough topography to produce detritus (Fig. 9a). Detrital path D_2 highlights faster exhumation of the EC that initiated 20–18 Myr ago and lasted at least until the Pliocene at a nearly constant rate between 0.3 and 0.6 mm yr^{-1}. Palaeocurrent indicators (Starck & Anzótegui, 2001), sandstone petrography and apatite fission-track data (Deeken *et al*., 2004; A. Deeken, E.R. Sobel, I. Coutand, M. Haschke, U. Riller & M.R. Strecker, submitted) suggest that the adjacent Cumbres de Luracatao (Fig. 2a) was being exhumed and eroded at that time. Uplift was accommodated by a north–south striking, west-dipping reverse fault on the eastern side of the range (Fig. 2a). The evolution of the compressional Angastaco basin began when sufficient accommodation space had been created in the footwall of the Luracatao thrust to accumulate and preserve erosional products from this range and other sources. If our interpretation of the detrital path D_3 is correct, and that a topography-creating exhumation event in the EC commenced in the late Eocene–early Oligocene, then the former foreland basin must have been segmented as it was farther west in the Puna in the Sierra de Calalaste-Salar de Antofalla area (Carrapa *et al*., 2005). Subsidence in the Angastaco basin accelerated at about 15 Ma (Fig. 9b). Our sandstone petrography data confirm that the EC must have constituted an efficient orographic barrier, because it was able to prevent transport of detritus derived from widely outcropping volcanics of the Puna plateau into the Angastaco basin (Figs 1a, 5 and 9b). During sediment deposition between ~15 and 9 ± 1 Ma, the climatic conditions are interpreted to have been arid (Starck & Anzótegui, 2001) as would be expected at this latitude (R. Alonso, B. Carrapa, I. Coutand, M. Haschke, G.E. Hilley,

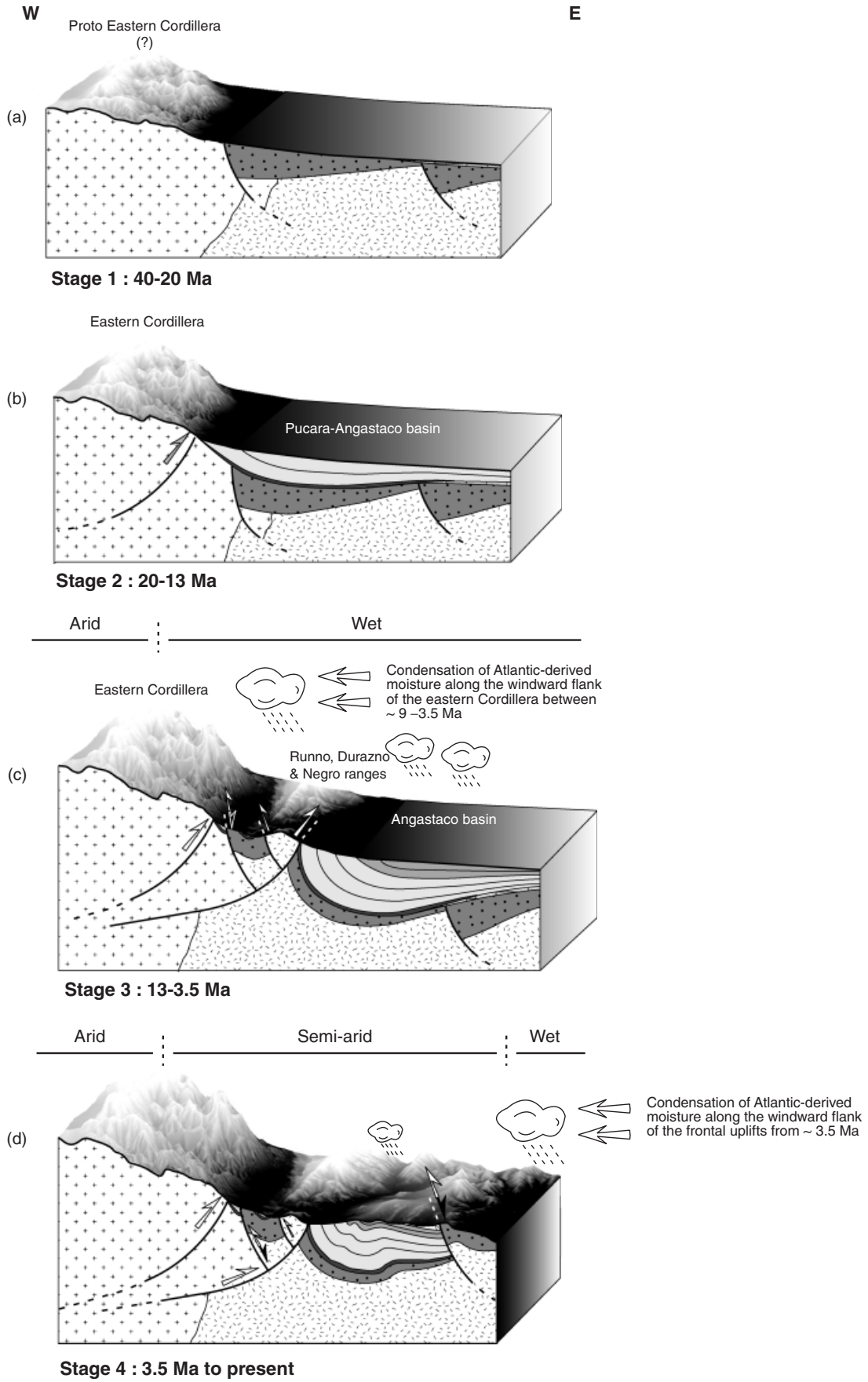

Fig. 9. Cartoons illustrating the tectonic, topographic and climatic evolution of the Eastern Cordillera and Calchaquí valley at the latitude of the Angastaco basin, during the last 40 Myr.

E.R. Sobel, M.R. Strecker & M.H. Trauth, submitted). This assessment is also compatible with oxygen-isotope data from the Corral Quemado basin located further south, in the Sierras Pampeanas province (Latorre *et al*., 1997).

During or right after the deposition of the Angastaco Formation, regional shortening shifted eastward, driving the exhumation of the Runno, Durazno and Negro Ranges (Figs 2a and 9c); this led to compartmentalization in the Pucara and Luracatao valleys to the west, and the modern Angastaco basin to the east. The late Cretaceous AFT ages obtained by Deeken *et al*. (2004) and A. Deeken, E.R. Sobel, I. Coutand, M. Haschke, U. Riller & M.R. Strecker (submitted) across these ranges indicate that the magnitude of exhumation is less than in the Luracatao Range. The increasing contribution of the D_5 detrital population to over 50% of the apatite fraction from sample AI16 (top of the Angastaco Formation, see Table 4 and Fig. 3) and an increased contribution of low-grade metamorphic detritus constituting these ranges (Fig. 5b) support the onset of exhumation in the Runno, Durazno and Negro Ranges between 13 and 10 Ma.

Depositional environments changed drastically between the deposition of the Angastaco and Palo Pintado Formations after about 9 Ma (Fig. 3) (Marshall *et al*., 1983; Starck & Anzótegui, 2001). The Palo Pintado and basal San Felipe Formations contain a rich fossil mammal fauna, freshwater mollusc fossils, pollen, leaves and tree-trunk remnants (e.g. Anzótegui, 1998; Starck & Anzótegui, 2001), from which a warm, humid forested environment, similar to the present foreland (e.g. Vergani & Starck, 1989; Starck & Vergani, 1996), can be inferred for the late Miocene to early Pliocene. In contrast, intramontane basins within the present Puna record sustained aridity and evaporite deposition at that time (Alpers & Brimhall, 1988; Alonso *et al*., 1991; Alonso, 1992; Vandervoort *et al*., 1995). These observations document that between about 9 and 5 Ma, the EC had reached a threshold elevation that forced precipitation from easterly sources, independent of global changes inferred from palaeo-temperatures (Starck & Anzótegui, 2001; R. Alonso, B. Carrapa, I. Coutand, M. Haschke, G.E. Hilley, E.R. Sobel, M.R. Strecker & M.H. Trauth, submitted) (Fig. 9c). Similar results were obtained from stable isotope analysis of palaeosols in the adjacent Santa Maria valley (Kleinert & Strecker, 2001) (Fig. 1).

In the late Pliocene, during deposition of the upper part of the San Felipe Formation, major changes in provenance and climatic conditions recurred. Palaeocurrent and provenance data indicating westward transport (Starck & Anzótegui, 2001) of sediments derived from the Sierra de los Colorados to the east (Fig. 2a and b) mark the onset of activity along a N–S striking, east-dipping thrust fault bounding the western flank of the Sierra. The uplift of this range (present-day elevation of 3500 m) coincided with a changeover to arid conditions in the Angastaco basin and the formation of calcretes sometime between 5.4 and 2.4 Ma (Fig. 9d), a scenario identical to the situation recorded in the Santa Maria basin to the south (Fig. 1) (Strecker *et al*., 1989; Kleinert & Strecker, 2001). This environmental change was accompanied by the deformation and exhumation of the entire Angastaco sedimentary sequence, the establishment of transient internal drainage conditions and the deposition of massive conglomerates with interfingered lacustrine sediments. In agreement with Starck & Anzótegui (2001), we propose that the late Pliocene uplift of the Sierras de los Colorados to the east created an orographic barrier that subsequently led to the aridification of the Calchaquí valley, by forcing Atlantic-derived moisture to condense along the windward flank of this then frontal foreland uplift (Fig. 9d).

CONCLUSIONS

Sandstone petrography, structural and stratigraphic analysis combined with detrital thermochronology in the intramontane Angastaco basin provide valuable information on the late Eocene to late Pliocene exhumation history of the eastern border of the Puna plateau and the successive establishment of orographic barriers along the southeastern flank of the Central Andes. Long-term exhumation rates based on detrital thermochronology revealed an increase from 0.1 to 0.3 mm yr^{-1} from late Eocene–Oligocene through Pliocene. However, the Luracatao Range in the EC was exhumed at a nearly constant rate between 0.3 and 0.6 mm yr^{-1} from the early Miocene (20–18 Ma) until the Pliocene. This created sufficient crustal thickening to initiate the Pucara-Angastaco compressional basin at about 15 Ma, when clastic material eroded from the EC began to be preserved. Apparently, by this time, the EC had undergone sufficient surface uplift to disrupt the fluvial network, disconnecting the interior of the Puna plateau from the foreland. By *ca*. 13–10 Ma, compressional deformation had shifted eastward, dividing the early basin into two subordinate depocentres: the Pucara valley to the west and the Angastaco basin to the east.

From about 15 to 9 Ma, the Angastaco Formation accumulated in the Angastaco basin under arid conditions. The overlying Palo Pintado Formation marks a drastic environmental change from a dry to a humid climate, similar to conditions in the Chaco lowlands and the Subandean ranges (Vergani & Starck, 1989; Starck & Vergani, 1996). At the same time, arid conditions characterized the Puna plateau to the west. This suggests that between about 9 and 5 Ma, the EC had built sufficient topography to focus Atlantic-derived precipitation and block moisture transport toward the Puna plateau.

In the late Pliocene (3.4–2.4 Ma), shortening was transferred to the eastern flank of the Angastaco basin, building another orographic barrier further east and establishing semi-arid conditions across the Calchaquí Valley. Along the southeastern flank of the Central Andes, the migration of compressional deformation and coeval building of orographic barriers in an environment with an easterly moisture source thus focused precipitation onto the windward (eastern) flanks of uplifts and starved the western hinterland of moisture.

The tectonic and climatic conditions in the southern Central Andes have led to an interesting relationship between tectonics and climate, where the eastward migration of deformation has been accompanied by successive aridification in the same direction. This evolution caused the tectonic defeat of fluvial systems by tectonically driven surface uplift, resulting in inefficient mass removal from the interior of the orogen (Sobel *et al*., 2003), and helped to preserve and aerially expand the internal drainage conditions of the Puna plateau.

ACKNOWLEDGEMENTS

This project is part of Collaborative Research Center (SFB) 267, 'Deformationsprozesse in den Anden', funded by the German Research Council (DFG) to M. Strecker. I. Coutand and B. Carrapa thank the Alexander von Humboldt Foundation for providing funding during their stay in Germany. The ion microprobe facility at UCLA is partly supported by a grant from the Instrumentation and Facilities Programme, Division of Earth Sciences, National Science Foundation. Simone Gaab is thanked for assistance in the field, S. Bonnet for providing Fig. 1b and G.E. Hilley for Fig. 1c. Constructive reviews by F.M. Dávila, P.G. DeCelles and P.A. van der Beek helped to improve the manuscript.

REFERENCES

Adelmann, D. (2001) Känozoische Beckenentwicklung in der südlichen Puna am Beispiel des Salar de Antofolla (NW-Argentinien). PhD Thesis, Frei Universität Berlin, Berlin, 180 pp.

Allmendinger, R.W., Jordan, T.E., Kay, S.M. & Isacks, B.L. (1997) The evolution of the Altiplano-Puna plateau of the central Andes. *Annu. Rev. Earth Planet. Sci.*, **25**, 139–174.

Alonso, R. (1992) Estratigrafía del Cenozoico de la cuenca Pastos Grandes (Puna Salteña) con énfasis en la Formación Sijes y sus boratos. *Rev. Asoc. Geol. Argentina*, **47**, 189–199.

Alonso, R.N., Jordan, T.E., Tabutt, K.T. & Vandervoort, D.S. (1991) Giant evaporite belts of the Neogene central Andes. *Geology*, **19**, 401–404.

Alpers, C.N. & Brimhall, G.H. (1988) Middle Miocene climatic change in the Atacama Desert, northern Chile; evidence from supergene mineralization at La Escondida. *Geol. Soc. Am. Bull.*, **100**(10), 1640–1656.

Andriessen, P.A.M. & Reutter, K.J. (1994) K–Ar and fission track mineral age determination of igneous rocks related to multiple magmatic arc systems along the 23°S latitude of Chile and NW Argentina. In: *Tectonics of the Southern Central Andes* (Ed. by K.-J. Reutter, E. Scheuber & P. Wigger), pp. 141–153. Springer, Berlin.

Anzótegui, L.M. (1998) Hojas de Angiospermas de la Formación Palo Pintado, Mioceno superior, Salta, Argentina, Parte I: Anacardiaceae, Lauraceae y Moraceae. *Ameghiniana*, **35**(1), 25–32.

Basu, A. (1976) Petrology of Holocene fluvial sand derived from plutonic source rocks: implication to paleoclimatic interpretation. *J. Sedim. Petrol.*, **46**, 694–709.

Batt, G.E. & Brandon, M.T. (2002) Lateral thinking: 2-D interpretation of thermochronology in convergent orogenic settings. *Tectonophysics*, **349**, 185–201.

Bernet, M., Zattin, M., Garver, J.I., Brandon, M.T. & Vance, J.A. (2001) Steady-state exhumation of the European Alps. *Geology*, **29**, 35–38.

Bianchi, A.R. & Yañez, C.E. (1992) Las precipitaciones en el noroeste Argentino: Salta, Instituto Nacíonal de Tecnología Agropecuaria, Estacíon Agropecuaria, 35pp.

Bianucci, H., Acevedo, O. & Cerdan, J. (1981) Evolución tectosedimentaria del Grupo Salta en la subcuenca Lomas de Olmedo (Provincias de Salta y Formaso). *Congr. Geol. Argent.*, **VIII**, 159–172.

Blackwell, D.D. & Steele, J.L. (1988) Thermal conductivity of sedimentary rocks: measurement and significance. In: *Thermal History of Sedimentary Basins – Methods and Case Histories* (Ed. by N.D. Naeser & T.H. McCulloh), pp. 13–36. Springer, Berlin.

Bossi, G.E., Georgieff, S.M., Gavriloff, I.J.C., Ibáñez, L.M. & Muruaga, C.M. (2001) Cenozoic evolution of the intramontane Santa Maria basin, Pampean Ranges, northwestern Argentina. *J. South Am. Earth Sci.*, **14**, 725–734.

Brandon, M.T. (1992) Decomposition of fission-track grain-age distributions. *Am. J. Sci.*, **292**, 535–564.

Brandon, M.T. (1996) Probability density plots for fission-track age distributions. *Rad. Meas.*, **26**, 663–676.

Brandon, M.T. (2002) Decomposition of mixed grain age distributions using binomfit. *On Track*, **24**, 13–18.

Brandon, M.T., Roden-Tice, M.K. & Garver, J.I. (1998) Late Cenozoic exhumation of the Cascadia accretionary wedge in the Olympic Mountains, northwest Washington State. *Geol. Soc. Am. Bull.*, **110**, 985–1009.

Braun, J. (2002) Estimating exhumation rate and relief evolution by spectral analysis of age-elevation datasets. *Terra Nova*, **14**, 210–214.

Brewer, I.D., Burbank, D.W. & Hodges, K.V. (2003) Modelling detrital cooling-age populations: insights from two Himalayan catchments. *Basin Res.*, **15**, 305–320.

Carrapa, B., Adelmann, D., Hilley, G.E., Mortimer, E., Sobel, E.R. & Strecker, M.R. (2005) Oligocene range uplift and development of plateau morphology in the southern Central Andes. *Tectonics*, **24**, TC4011. doi:10.1029/2004TC001762.

Cerveny, P.F., Naeser, N.D., Zeitler, P.K., Naeser, C.W. & Johnson, N.M. (1988) History of uplift and relief of the Himalaya during the past 18 million years; evidence from sandstones of the Siwalik Group. In: *New Perspectives in Basin Analysis* (Ed. by K.L. Kleispehn & C. Paola), pp. 43–61. Springer-Verlag, Berlin.

Compston, W., Williams, I.S. & Meyer, C. (1984) U–Pb geochronology of zircons from lunar breccia 73217 using a sensitive high mass-resolution ion microprobe. *J. Geophys. Res.*, **89**(Suppl.), B525–B534.

Coughlin, T.J., O'Sullivan, P.B., Kohn, B.P. & Holcombe, R.J. (1998) Apatite fission-track thermochronology of the Sierras Pampeanas, central western Argentina; implications for the mechanism of plateau uplift in the Andes. *Geology*, **26**(11), 999–1002.

Coutand, I. (1999) Tectonique cénozoïque du haut plateau de la Puna, Nord-Ouest argentin, Andes Centrales. PhD, Université de Rennes 1.

Coutand, I., Cobbold, P.R., de Urreiztieta, M., Gautier, P., Chauvin, A., Gapais, D., Rossello, E.A. & López-Gamundí, O. (2001) Style and history of Andean deformation,

Puna plateau, northwestern Argentina. *Tectonics*, **20**(2), 210–234.

Deeken, A.D., Sobel, E.R., Haschke, M.R., Strecker, M.R. & Riller, U. (2004) Age of initiation and growth pattern of the Puna Plateau, NW-Argentina, constrained by AFT thermochronology. In *10th International Fission Track 2004 Conference*, Amsterdam.

Deming, D., Nunn, J.A. & Evans, D.G. (1990) Thermal effects of compaction-driven groundwater flow from overthrust belts. *J. Geophys. Res.*, **95**(5), 6669–6683.

DiGiulio, A. (1990) Litostratigrafia e petrografia della successione Eo-Oligocenica del Bacino Terziario Ligure-Piemontese nell'area compresa tra le Valli Grue e Curone (provincia di Alessandria, Italia Settentrionale). *Boll. Soc. Geol. Ital.*, **109**, 279–298.

DiGiulio, A. & Valloni, R. (1992) Sabbie e areniti, analisi ottica e classificazione. *Acta Nat.*, **28**, 55–101.

Dickinson, W.R. (1970) Interpreting detrital modes of greywacke and arkose. *J. Sedim. Petrol.*, **40**, 695–707.

Donelick, M.B., Ketcham, R.A. & Carlson, W.D. (1999) Variability of apatite fission-track annealing kinetics: II. Crystallographic orientation effects. *Am. Mineral.*, **84**, 1224–1234.

Dumitru, T.A. (1993) A new computer-automated microscope stage system for fission track analysis. *Nucl. Tracks Radiat. Meas.*, **21**, 575–580.

Dunkl, I. (2002) Trackkey: *windows program for calculation and graphical presentation of EDM fission track data*, version 4.2: http://www.gzg.uni-goettingen.de/forschung/abt_sediment/sed_mitarb/website_id/softwares/trackkey.html.

Durand, F. (1992) Avances y problemas en la definición del límite Precámbrico-Cámbrico en el Noroeste Argentino. In: *El Paleozoico Inferior en Latinoamerica y la Génesis del Gondwana* (Univ. Nacl Tucumán **9**, 127–138.

Díaz, J.I. & Malizzia, D.C. (1983) Estudio geológico y sedimentológico del Terciario Superior del valle Calchaquí (departamento de San Carlos, provincia de Salta). *Bol. Sedimentol.*, **2**, 8–28.

Díaz, J.I., Malizzia, D.C. & Bossi, G.E. (1987) Análisis estratigráfico y sedimentológico del Grupo Payogastilla (Terciario superior). *Dec. Congr. Geol. Argent.*, 113–117.

Díaz, J.I. & Miserendino Fuentes, A. (1988) El ambito deposicional y tectonico del Grupo Payogastilla (Provincia de Salta, Republica Argentina). *Congr. Geol. Chil.*, **39**, 87–103.

Folk, R.L. (1968) *Petrology of Sedimentary Rocks*. Hemphill Publishing Co., Austin, TX, 182pp.

Galbraith, R.F. (1981) On statistical models for fission track counts. *Math. Geol.*, **13**, 471–478.

Galbraith, R.F. & Green, P.F. (1990) Estimating the component ages in a finite mixture. *Nucl. Tracks Radiat. Meas.*, **17**, 197–206.

Gallagher, K. (1995) Evolving temperature histories from apatite FT data. *Earth Planet. Sci. Lett.*, **136**, 421–435.

Garven, G. (1989) A hydrogeologic model for the formation of the giant oil sands deposits of the Western Canada sedimentary basin. *Am. J. Sci.*, **289**, 105–166.

Garver, J.I., Brandon, M.T., Roden-Tice, M. & Kamp, P.J.J. (1999) Exhumation history of orogenic highlands determined by detrital fission-track thermochronology. In: *Exhumation Processes: Normal Faulting, Ductile Flow and Erosion* (Ed. by U. Ring, M.T. Brandon, G.S. Lister & S.D. Willett), *Geol. Soci. Lond.*, **154**, 283–304.

Gazzi, P. (1966) Le arenarie del Flysh opra-cretaceo dell'Appennino modenese; correlazioni con il Flysh di Monghidoro. *Mineral. Petrogr. Acta*, **12**, 69–97.

Gleadow, A.J.W. & Duddy, I.R. (1981) A natural long-term annealing experiment for apatite. *Nucl. Tracks*, **5**, 169–174.

Green, P.F. (1981) A new look at statistics in fission track dating. *Nucl. Tracks Radiat. Meas.*, **5**, 77–86.

Green, P.F., Duddy, I.R., Gleadow, A.J.W. & Tingate, P.R. (1985) Fission track annealing in apatite: track length measurements and the form of the Arrhenius plot. *Nucl. Tracks Radiat. Meas.*, **10**, 323–328.

Green, P.F., Duddy, I.R., Gleadow, A.J.W., Tingate, P.R. & Laslett, G.M. (1986) thermal annealing of fission tracks in apatite, 1. A qualitative description. *Chem. Geol.*, **59**, 237–253.

Grier, M.E. (1990) The influence of the Cretaceous Salta rift basin on the development of andean structural geometries. PhD, Cornell University, NW Argentine Andes.

Grier, M.E. & Dallmeyer, R.D. (1990) Age of the Payogastilla Group: implication for foreland basin development, NW Argentina. *J. South. Am. Earth Sci.*, **3**(4), 269–278.

Grier, M.E., Salfity, J.A. & Allmendinger, R.W. (1991) Andean reactivation of the Cretaceous Salta rift, northwestern Argentina. *J. South Am. Earth Sci.*, **4**(4), 351–372.

Hartley, A.J. (2003) Andean uplift and climate change. *J. Geol. Soc. Lond.*, **160**(1), 7–10.

Haselton, K., Hilley, G.E. & Strecker, M.R. (2002) Average Pleistocene climatic patterns in the southern central Andes: controls on mountain glaciation and paleoclimate implications. *J. Geol.*, **110**, 211–226, doi: 10.1086/338414.

Hilley, G.E. & Strecker, M.R. (2004) Steady state erosion of critical Coulomb wedges with applications to Taiwan and the Himalaya. *J. Geophys. Res.*, **109**, B01411. doi:10.1029/2002JB002284.

Hilley, G.E. & Strecker, M.R. (2005) Processes of oscillatory basin filling and excavation in a tectonically active orogen: Quebrada del Toro Basin, NW Argentina. *Geol. Soc. Am. Bull.*, **117**(7/8), 887–901.

Hongn, F., Seggiaro, R. & Ramalio, E. (1999) Cachi, 2566-III. SEGEMAR, Instituto de Geologia y Recursos Minerales.

Horton, B.K. (2005) Revised deformation history of the central Andes: inferences from Cenozoic foredeep and intermontane basins of the Eastern Cordillera, Bolivia. *Tectonics*, **24**, TC3011. doi :10.1029/2003TC001619.

Horton, B.K., Hampton, B.A., LaReau, B.N. & Baldellòn, E. (2002) Tertiary provenance history of the northern and central Altiplano (Central Andes, Bolivia): a detrital record of the plateau-margin tectonics. *J. Sed. Res.*, **72**(5), 711–726.

Hurford, A.J. (1986) Cooling and uplift patterns in the Lepontine Alps, South Central Switzerland and an age of vertical movement on the Insubric fault line. *Contrib. Mineral. Petrol.*, **92**, 413–427.

Hurford, A.J. (1990) Standardization of fission-track dating calibration: recommendation by the Fission Track Working Group of the I.U.G.S. Subcommission on geochronology. *Chem. Geol.*, **80**, 171–178.

Hurford, A.J. & Green, P.F. (1983) The zeta age calibration of fission-track dating. *Isot. Geosci.*, **1**, 285–317.

Ingersoll, R.V., Bullard, T.F., Ford, R.L., Grimm, J.P. & Pickle, J.D. (1984) The effect of grain size on detrital modes: a test of the Gazzi–Dickinson point-counting method. *J. Sedim. Petrol.*, **54**(1), 103–116.

Isacks, B.L. (1988) Uplift of the Central Andean Plateau and bending of the Bolivian Orocline. *J. Geophys. Res.*, **93**(B4), 3211–3231.

Jordan, T.E. & Alonso, R.N. (1987) Cenozoic stratigraphy and basin tectonics of the Andes Mountain, 20–28° South latitude. *Am. Assoc. Petrol. Geol. Bull.*, **71**(1), 49–64.

Jordan, T.E., Reynolds, J.H. & Erikson, J.P. (1997) Variability in age of initial shortening and uplift in the central Andes, 16–33°30′S. In: *Tectonic Uplift and Climate Change* (Ed. by W.F. Ruddiman), pp. 41–61. Plenum Press, New York.

Kay, S.M., Coira, B. & Viramonte, J. (1994) Young mafic back-arc volcanic rocks as indicators of continental lithospheric delamination beneath the Argentine Puna Plateau, Central Andes. *J. Geophys. Res.*, **99**, 24323–24340.

Ketcham, R.A., Donelick, R.A. & Carlson, W.D. (1999) Variability of apatite fission-track annealing kinetics: III. Extrapolation to geological time scales. *Am. Mineral.*, **84**, 1235–1255.

Ketcham, R.A., Donelick, R.A. & Donelick, M.B. (2000) AFTSolve: a program for multi-kinetic modeling of apatite fission-track data. *Geol. Mat. Res.*, **2**(1), 1–32.

Kleinert, K. & Strecker, M.R. (2001) Climate change in response to orographic barrier uplift: paleosol and stable isotope evidence from the late Neogene Santa Maria basin, northwestern Argentina. *Geol. Soc. Am. Bull.*, **113**(6), 728–742.

Kley, J. & Monaldi, C.R. (1998) Tectonic shortening and crustal thickness in the Central Andes: how good is the correlation ? *Geology*, **26**, 723–726.

Kraemer, B., Adelmann, D., Alten, M., Schnurr, W., Erpenstein, K., Kiefer, E., van den Bgaard, P. & Görler, K. (1999) Incorporation of the Paleogene foreland into Neogene Puna plateau: the Salar de Antofalla, NW Argentina. *J. South Am. Earth Sci.*, **12**, 157–182.

Lamb, S., Hoke, L., Kennan, L. & Dewey, J. (1997) Cenozoic evolution of the Central Andes in Bolivia and northern Chile. In: *Orogeny Through Time* (Ed. by J.-P. Burg & M. Ford), *Geol. Soc. Spec. Publ.*, **121**, 237–264.

Laslett, G.M. & Galbraith, R.F. (1996) Statistical modelling of thermal annealing of fission tracks in apatite. *Geochim. Cosmochim. Acta*, **60**, 5117–5131.

Laslett, G.M., Green, P.F., Duddy, I.R. & Gleadow, A.J.W. (1987) Thermal annealing of fission tracks in apatite. A quantitative analysis. *Chem. Geol. (Isot. Geosci. Sect.)*, **65**, 1–13.

Latorre, C., Quade, J. & McIntosh, W.C. (1997) The expansion of C-4 grasses and global change in the late Miocene: stable isotopes evidence from the Americas. *Earth Planet. Sci. Lett.*, **146**, 83–96.

Lork, A. & Bahlburg, H. (1993) Precise U–Pb ages of monazites from the Faja Eruptiva de la Puna Oriental and the Cordillera Oriental, NW Argentina. *XII Congr. Geol. Argent. II Congr. Expl. Hidrocarburos*, **12**, 1–6.

Lork, A., Miller, H. & Kramm, U. (1990) U–Pb zircon and monazite ages of the Angostura granite and the orogenic history of the northwest Argentine basement. *J. South Am. Earth Sci.*, **2**, 147–153.

Maksaev, V. & Zentilli, M. (1999) Fission track thermochronology of the Domeyko Cordillera, northern Chile: implications for Andean tectonics and porphyry copper metallogenesis. *Expl. Mining Geol.*, **8**, 65–89.

Mancktelow, N.S. & Grasemann, B. (1997) Time-dependent effects of heat advection on topography and cooling histories during erosion. *Tectonophysics*, **270**, 167–195.

Marquillas, R.A., del Papa, C. & Sabino, I.F. (2005) Sedimentary aspects and paleoenvironmental evolution of a rift basin: salta Group (Cretaceous–Paleogene), northwestern Argentina. *Int. J. Earth Sci.*, **94**(1), 94–113.

Marrett, R.A. & Strecker, M.R. (2000) Response of intracontinental deformation in the central Andes to late Cenozoic reorganization of South American Plate motions. *Tectonics*, **19**, 452–467.

Marshall, L.G., Hoffstetter, R. & Pascual, R. (1983) Mammals and stratigraphy: geochronology of the continental mammal-bearing Tertiary of South America. *Palaeovertebrata*, Special Volume, 93.

Masek, J.G., Isacks, B.L., Gubbels, T.L. & Fielding, E.J. (1994) Erosion and tectonics at the margins of continental plateaus. *J. Geophys. Res.*, **99**(B7), 13941–13956.

McQuarrie, N. (2002) The kinematic history of the central Andean fold-thrust belt, Bolivia: implications for building a high plateau. *Geol. Soc. Am. Bull.*, **114**(8), 950–963.

Miller, D.S., Duddy, I.R., Green, P.F., Hurford, A.J. & Naeser, C.W. (1985) Results of interlaboratory comparison of fission-track age standards. *Nucl. Tracks Radiat. Meas.*, **10**, 381–391.

Mon, R. & Salfity, J.A. (1995) Tectonic evolution of the Andes of northern Argentina. In: *Petroleum Basins of South America* (Ed. by A.J. Tankard, R.S. Soruco & H.J. Welsink), *Am. Assoc. Petrol. Geol. Mem.*, **62**, 269–283.

Muruaga, C.M. (2001a) Estratigrafía y desarrollo tectosedimentario de los sedimentos terciarios en los alrededores de la Sierra de Hualfín, borde suroriental de la Puna, Catamarca, Argentina. *Assoc. Argent. Sedimentol.*, **8**(1), 27–50.

Muruaga, C.M. (2001b) Petrografía y procedencia de areniscas terciarias en la Subcuenca de Hualfín, provincia de Catamarca, noroeste de Argentina. *Assoc. Argent. Sedimentol.*, **8**(2), 15–35.

Méndez, V., Navarini, A., Plaza, D. & Viera, O. (1973) Faja Eruptiva de la Puna Oriental. *Congr. Geol. Argent.*, 89–100.

Naeser, C.W. (1976) Fission track dating, U.S. Geological Survey, p. 65.

Omarini, R.H., Sureda, R.J., Götze, H.J., Seilacher, A. & Pflüger, F. (1999) Puncoviscana folded belt in northwestern Argentina: testimony of Late Proterozoic Rodinia fragmentation and pre-Gondwana collisional episodes. *Int. J. Earth Sci.*, **88**, 76–97.

Omarini, R.H., Viramonte, J.G., Cordani, U., Salfity, J.A. & Kawashita, K. (1984) Estudio geocronológico Rb/Sr de la Faja Eruptiva de la Puna en el sector de San Antonio de los Cobres, Provincia de Salta, Argentina. *Noveno Congr. Geol. Argent.*, 146–158.

Paces, J.B. & Miller, J.D. (1993) Precise U–Pb ages of Duluth complex and related mafic intrusions, northeastern Minnesota; geochronological insights to physical, petrogenetic, paleomagnetic, and tectonomagnetic processes associated with the 1.1 Ga Midcontinent Rift System. *J. Geophys. Res.*, **98**, 13997–14013.

Ruiz, P.S. (1993) Estudio geológico en el valle de Pucara, Departamento San Carlos, Provincia de Salta. Tesis Profesional, Universidad Nacíonal de Salta.

Ruiz, G.M.H., Seward, D. & Winkler, W. (2004) Detrital thermochronology – a new perspective on hinterland tectonics, an example from the Andean Amazon Basin, Ecuador. *Basin Res.*, **16**, 413–430.

Salfity, J.A., Gorustovich, S.A., Moya, M.C. & Amengual, R. (1984) Marco tectónico de la sedimentación y efusividad Cenozoicas en la Puna Argentina. *Congr. Geol. Argentino*, **IX**, 539–554.

Salfity, J.A. & Marquillas, R.A. (1994) Tectonic and sedimentary evolution of the Cretaceous-Eocene Salta Group basin, Argentina. In: *Cretaceous Tectonics of the Andes* (Ed. by J.A. Salfity), pp. 266–315. Fried. Vieweg & Sohn, Germany.

Sañudo-Wilhelmy, S.A. & Flegal, A.R. (1994) Temporal variations in lead concentrations and isotopic composition in the

Southern California Bight. *Geochim. Cosmochim. Acta*, **58**, 3315–3320.

Schmitt, A.K., Grove, M., Harrison, T.M., Lovera, O., Hulen, J.B. & Walters, M. (2002) The Geysers–Cobb Mountain System, California. (Part 1): U–Pb zircon ages of volcanic rocks, conditions of zircon crystallization and magma residence times. *Geochim. Cosmochim. Acta*, **67**, 3423–3442.

Sobel, E.R., Hilley, G.E. & Strecker, M.R. (2003) Formation of internally drained contractional basins by aridity-limited bedrock incision. *J. Geophys. Res.*, **108**(B7), 2344. doi:10.1029/2002JB001883.

Sobel, E.R. & Strecker, M.R. (2003) Uplift, exhumation and precipitation: tectonic and climatic control of Late Cenozoic landscape evolution in the northern Sierras Pampeanas, Argentina. *Basin Res.*, **15**, 431–451.

Springer, M. & Förster, A. (1998) Heat-flow density across the Central Andean subduction zone. *Tectonophysics*, **291**, 123–139.

Starck, D. & Anzótegui, L.M. (2001) The late miocene climatic change – persistence of a climatic signal through the orogenic stratigraphic record in northwestern Argentina. *J. S. Am. Earth Sci.*, **14**, 763–774.

Starck, D. & Vergani, G. (1996) Desarrollo Tecto-sedimentario del Cenozoico en el Sur de la provincia de Salta-Argentina. *13 Congr. Geol. Argent. Tercero Congr. Expl. Hidrocarburos*, **13**, 433–452.

Strecker, M.R., Cerveny, P., Bloom, A.L. & Malizzia, D. (1989) Late tectonism and landscape development in the foreland of the Andes: Northern Sierras Pampeanas (26–28°S), Argentina. *Tectonics*, **8**(3), 517–534.

Stüwe, K., White, L. & Brown, R. (1994) The influence of eroding topography on steady-state isotherms: application to fission track analysis. *Earth Planet. Sci. Lett.*, **124**, 63–74.

Toselli, A. (1990) Metamorfismo del Ciclo Pampeano. In: *El Ciclo Pampeano en el Noroeste Argentino* (Ed. by F.G. Aceñolaza, H. Miller & A.J. Toselli), *Univ. Nac. Tucumán*, **4**, 181–197.

Turner, J.C.M. (1960) Estratigrafía del Nevado de Cachi y sector al oeste. *Acta Geol. Lilloana Tucumán*, **3**, 191–226.

Valloni, R. (1985) Reading provenance from modern marine sands. In: *Provenance of Arenites* (Ed. by G.G. Zuffa), *NATO-ASI Ser.,* **148**, 309–332.

Vandervoort, D.S., Jordan, T.E., Zeitler, P.K. & Alonso, R.N. (1995) Chronology of internal drainage development and uplift, southern Puna plateau, Argentine central Andes. *Geology*, **23**(2), 145–148.

Vergani, G. & Starck, D. (1989) Geología del Sur de la Provincia de Salta – Parte II: Estratigrafía y evolución tectosedimentaria del Cenozoico entre el Valle Calchaquí y Metán, Unpublished. Y.P.F.

Wiedenbeck, M., Alle, P., Corfu, F., Griffin, W.L., Meier, M., Oberli, F., Von Quadt, A., Roddick, J.C. & Spiegel, W. (1995) Three natural zircon standards for U–Th–Pb, Lu–Hf, trace element and REE analyses. *Geostand. Newslett.*, **91**, 1–23.

Willett, S.D., Issler, D., Beaumont, C., Donelick, R.A. & Grist, A. (1997) Inverse modeling of annealing of fission tracks in apatite 2; application to the thermal history of the Western Canada Sedimentary Basin. *Am. J. Sci.*, **297**, 970–1011.

World Meteorological Organization (WMO) (1975) Climatic atlas of South America: World Meteorological Organization, Geneva, scale 1:1,000,000, 28pp.

Manuscript received 26 May 2005; Manuscript accepted 19 January 2006.

